


**Effect of realistic out-of-plane dopant potentials on the superfluid density of overdoped cuprates**H. U. Özdemir,<sup>1</sup> Vivek Mishra<sup>2</sup>, N. R. Lee-Hone,<sup>1</sup> Xiangru Kong<sup>3</sup>, T. Berlijn<sup>3</sup>, D. M. Broun,<sup>1</sup> and P. J. Hirschfeld<sup>4</sup><sup>1</sup>*Department of Physics, Simon Fraser University, Burnaby, Canada BC V5A 1S6*<sup>2</sup>*Kavli Institute for Theoretical Sciences, University of Chinese Academy of Sciences, Beijing 100190, China*<sup>3</sup>*Center For Nanophase Materials Sciences, Oak Ridge National Laboratory, Oak Ridge, Tennessee 37831, USA*<sup>4</sup>*Department of Physics, University of Florida, Gainesville, Florida 32611, USA* (Received 6 June 2022; revised 3 October 2022; accepted 6 October 2022; published 18 November 2022)

Recent experimental papers on hole-doped overdoped cuprates have argued that a series of observations showing unexpected behavior in the superconducting state imply the breakdown of the quasiparticle-based Landau–BCS paradigm in that doping range. In contrast, some of the present authors have argued that a phenomenological “dirty  $d$ -wave” theoretical analysis explains essentially all aspects of thermodynamic and transport properties in the superconducting state, provided the unusual effects of weak, out-of-plane dopant impurities are properly accounted for. Here we attempt to place this theory on a more quantitative basis by performing *ab initio* calculations of dopant impurity potentials for LSCO and Tl-2201. These potentials are more complex than the pointlike impurity models considered previously, and require calculation of forward scattering corrections to transport properties. Including realistic, ARPES-derived band structures, Fermi liquid renormalizations, and vertex corrections, we show that the theory can explain semiquantitatively the unusual superfluid density measurements of the two most studied overdoped materials.

DOI: [10.1103/PhysRevB.106.184510](https://doi.org/10.1103/PhysRevB.106.184510)**I. INTRODUCTION**

Cuprates have represented a challenge to the central paradigms of condensed matter physics since their discovery in 1986 [1,2]. High-temperature superconductivity evolves with doping out of the Mott state together with a host of exotic and poorly understood phenomena such as the pseudogap phase, the strange metal phase and various intertwined orders, so it has been natural to formulate the problem as one of understanding the ground state of the doped Mott insulator. Indeed, there is general agreement that aspects of the underdoped phase diagram imply a definitive breakdown of the Landau–BCS quasiparticle-based approach to interacting electrons. On the other hand, an alternative philosophy consists in assuming that it is equally valid to attack the superconductivity problem from the overdoped side, where intertwined orders are largely absent and there is no pseudogap. It is assumed in such an approach that the Landau–BCS theory applies for sufficiently high doping  $p$ , implying that in the range of experimental interest between  $p \simeq 20$ –30% it should be a good starting point, with significant but perturbative corrections due to reduced quasiparticle weights, and residual quasiparticle interactions represented by Landau parameters.

Recently, this notion was challenged by several experiments on epitaxially grown overdoped LSCO films, closely spaced in doping. Papers reporting both superfluid density [3] and terahertz conductivity [4] measurements revealed strong deviations from naive expectations for a clean  $d$ -wave superconductor, and claimed furthermore that disorder could not explain these effects, primarily based on the observed linearity of the measured superfluid density. However, in a

series of papers [5–7], some of the present authors argued that accounting for the weak-scattering nature of the dominant out-of-plane dopant impurities, as well as the realistic low-energy electronic structure, could explain these observations. These works calculated, for the same set of phenomenological impurity parameters within the so-called “dirty  $d$ -wave” theory [8,9], not only superfluid density and optical conductivity, but also specific heat and thermal conductivity, concluding that the theory accounted well for the properties of the superconducting state in the overdoped regime of LSCO and Tl-2201 (crystal structures shown in Figs. 1 and 2), the two materials that have been systematically studied at high overdoping. Nevertheless, there has been an ongoing reluctance to accept that simple impurity models, based on pointlike defects and predominantly Born-limit scatterers, are applicable and operating in a physically relevant parameter regime [4,10].

Accounting semiquantitatively for differences among overdoped cuprate materials requires a detailed understanding of the dopant impurities themselves. In Refs. [5–7], overdoped cuprates were modeled by a 2D tight-binding band, and specifying a relatively weak onsite impurity potential, of order  $0.1t$ , where  $t$  is the nearest neighbor Cu–Cu hopping in the plane. But in real cuprates, the dopants and defect atoms are situated in various sites of the crystal, and may therefore be expected to produce quite different effective scattering potentials as experienced by electrons propagating in the  $\text{CuO}_2$  plane. For example, in LSCO, both the apical oxygen vacancies, and the Sr dopants that substitute for La at the so-called A site, are located only one layer away ( $0.5a$  away, where  $a$  is the in-plane lattice spacing) from the nearest  $\text{CuO}_2$  plane (Fig. 1). In Tl-2201, oxygen interstitials, and the excess Cu that

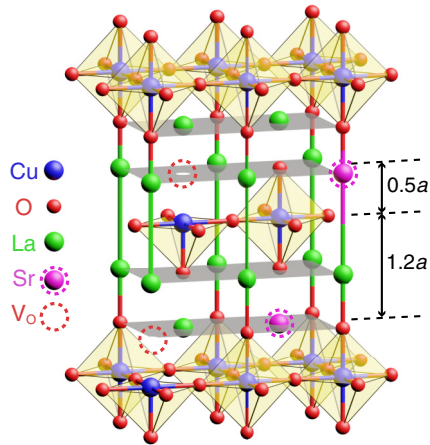


FIG. 1. Several unit cells of body-centered-tetragonal  $\text{La}_{2-x}\text{Sr}_x\text{CuO}_4$ , showing the location of the dominant defects: Sr dopants, substituting for La at the A site; and apical-oxygen vacancies,  $\text{V}_\text{O}$ . (Impurity locations are indicated by dashed circles.) Note that, as experienced by electrons propagating in the  $\text{CuO}_2$  planes, each defect plays a dual role: once for the closest  $\text{CuO}_2$  plane, located a distance  $0.5a$  away; and again for the more distant  $\text{CuO}_2$  plane, a distance  $1.2a$  away. The body-centered tetragonal structure means that in one case the impurity is site centered, and in the other plaquette centered. In particular, the apical-oxygen vacancy is centered directly above a Cu site, imparting significant pointlike character to its impurity potential, as we will see below.

substitutes for Tl [11], are located at least two layers ( $1.2a$ ) away, producing correspondingly weaker in-plane potentials [12,13] (Fig. 2). In addition to the effect on the magnitude of the potential, defects residing outside the  $\text{CuO}_2$  planes produce a longer-range scattering “footprint” in the  $\text{CuO}_2$  plane, which is particularly important for transport, where a predominance of forward scattering enhances the current. As we show below, the in-plane momentum dependence of the effective impurity potential is nontrivial, being determined by the projection of the impurity position onto the  $\text{CuO}_2$  plane. In particular, the nature of the scattering depends sensitively on whether the defect is site-centered or plaquette-centered with respect to the  $\text{CuO}_2$  lattice, as shown schematically in Fig. 3. (For the body-centered tetragonal structures shown in Figs. 1 and 2, each defect is simultaneously site-centered with respect to one neighboring  $\text{CuO}_2$  plane, and plaquette-centered—albeit at different distance—from its other neighboring  $\text{CuO}_2$  plane.) These factors all influence the strength and range of the potential, and in turn determine the degree of pairbreaking and the resulting anisotropy of the quasiparticle and transport scattering rates.

Recognizing the importance of apical oxygen vacancies in LSCO, a recent study has taken the first steps toward understanding the role of these defects in the overdoped cuprates [14]. Unfortunately, that work assumed an incorrect form for the impurity potential, stating without proof that the apical O vacancy has zero potential on the Cu site below it. In addition, the study did not carry out a self-consistent treatment of the self energy, using instead the normal-state form for the scattering rate. Furthermore, Ref. [14] neglected to consider forward-scattering corrections and explicit

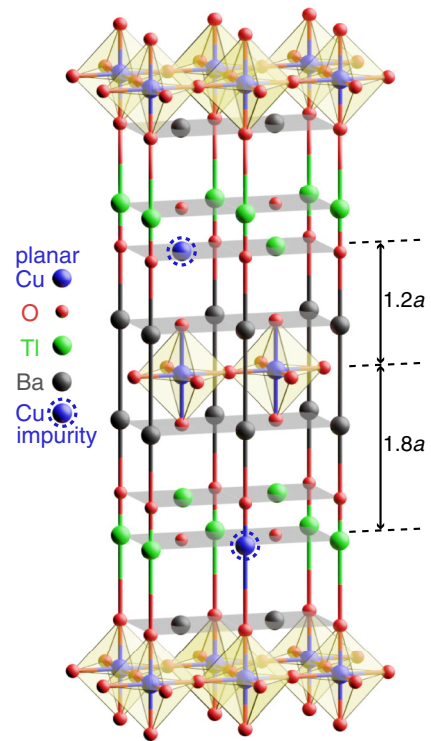


FIG. 2. Several unit cells of body-centered-tetragonal  $\text{Tl}_2\text{Ba}_2\text{CuO}_{4+\delta}$ . Tetragonal Tl-2201 naturally grows with an excess of Cu (indicated by dashed circles) that substitutes for Tl atoms in the  $\text{Tl}_2\text{O}_2$  double layers, and makes a significant contribution to the hole doping of this material [11]. As in LSCO, these copper defects play a dual role: simultaneously site-centered with respect to the nearest  $\text{CuO}_2$  plane and plaquette-centered with respect to the more distant one. (The  $\text{Tl}_2\text{O}_2$  double layers also host interstitial oxygen dopants, not shown here.) The large unit cell height of Tl-2201 means that these defects are located well away from the  $\text{CuO}_2$  planes (at least  $1.2a$ ), leading to weaker impurity potentials that have strong forward-scattering character.

gap renormalization, both of which are important when the impurity potential is momentum dependent, and have a significant effect on both the qualitative and quantitative behavior of the superconductivity and the electrodynamics. We discuss this work further in a separate comment [15].

Confirming the general dirty  $d$ -wave description of the overdoped cuprates thus requires a more accurate calculation of impurity potentials, including the vertex corrections to the transport properties that arise with extended impurity potentials. In this paper, we perform a series of *ab initio* calculations of the tight-binding impurity potentials due to various dopants and defects, including their local modification of the hopping parameters, using a Wannier-function-based supercell approach [16], and revisit the calculations of Refs. [5–7]. We also discuss the influence of band-structure effects, including the proximity in the overdoped regime of the van Hove singularity at the  $(\pi, 0)$  point, which necessitates the use of momentum sums rather than Fermi-surface integrals. We find that the success of the previous phenomenological approach is confirmed by the more complete *ab initio*-based calculations presented here.

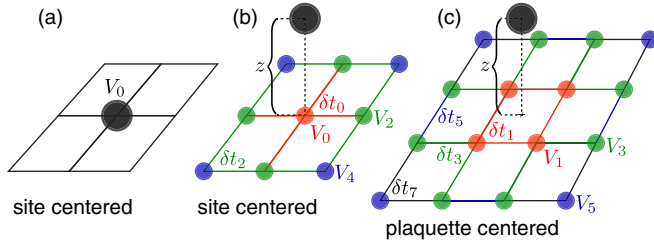


FIG. 3. A one-band model of the square  $\text{CuO}_2$  lattice, depicting the tight-binding impurity potential as experienced by an electron propagating in the  $\text{CuO}_2$  plane. Terms  $\delta H_{\text{RR}}^i$  in the impurity Hamiltonian, Eq. (1), that are equivalent by symmetry have been grouped, resulting in a sequence of site energies,  $V_i$ , and a hierarchy of modifications of the nearest-neighbor hopping integral,  $\delta t_i$ , which are listed in Tables I–III for the various impurities. (For clarity, modifications of the next-nearest-neighbor hopping integrals are not shown, but are also included in the model.) (a) An in-plane, site-centered defect, e.g., a Cu vacancy in the  $\text{CuO}_2$  plane, which we treat as a point scatterer with a single, on-site impurity term  $V_0$ ; (b) an out-of-plane, site-centered defect, e.g., an apical O vacancy, located a height  $z$  above the nearest Cu; and (c) an out-of-plane, plaquette-centered defect, e.g., a Sr substituting for La at an A site located a height  $z$  above the nearest  $\text{CuO}_2$  plaquette. Note that while a site-centered defect can be predominantly pointlike (i.e.,  $V_0 \gg V_2, V_4, \dots$ ), a plaquette-centered defect is always equidistant from its four closest Cu sites: it therefore has finite range and is inherently of forward-scattering character.

The nonuniversal details of the calculations may seem tedious to those interested in drawing broad conclusions for the generic cuprate phase diagram, but we regard them as essential to establishing the applicability of the quasiparticle-based Landau–BCS paradigm to the overdoped cuprates in the sense described above. We believe that it is important to investigate conventional explanations for the apparently unusual physics uncovered in Refs. [3,4] and other works before turning to more exotic explanations [17]. Conversely, if alternative theories beyond the Landau–BCS paradigm are put forward, then it seems reasonable to insist that they be capable of explaining the experimental data, and the variation of properties between different cuprates, at the same level of detail as presented here.

## II. FORMALISM

### A. Band structure

For our purposes here, an *ab initio* description of the effective impurity potentials is desired to convince the reader that a realistic, materials-specific description of overdoped cuprates has been obtained. Here one immediately encounters the usual challenge associated with describing cuprates by first principles approaches, namely that density functional theory (DFT) in its simplest form fails for the cuprate parent compounds because it cannot describe the Mott insulating state. While considerable progress has been made incorporating correlations into DFT to describe high-energy physics [18,19], these methods are not appropriate for a complete *ab initio* description of low-energy phenomena, accurate at the few meV level. We therefore adopt a hybrid approach,

starting with a low-energy tight-binding model describing the  $\text{CuO}_2$ -plane states of the notional pure material, with hopping matrix elements taken from fits to ARPES measurements on LSCO [20,21] and Tl-2201 [22]. To capture the continuous evolution of electronic structure with doping, tight-binding parameters for LSCO are interpolated between the fixed dopings at which the ARPES measurements were performed [20]. The only parameter with strong doping dependence is the chemical potential, which is set using the direct correspondence between hole doping and Fermi volume. The doping dependence of the next-nearest-neighbor hopping is relatively weak, and all other tight-binding parameters are doping independent. For Tl-2201, limited ARPES data [22] means that doping dependence of electronic structure is generated via rigid band-shift, with the only doping-dependent parameter the chemical potential. (For more details of the procedure see Refs. [5,7].)

The only additional renormalization that needs to be considered when modeling the pure electronic structure is the many-body renormalization that occurs close to the Fermi level, which flattens the dispersion  $\xi_{\mathbf{k}}$  by a factor of  $m/m^*$ . As discussed in Ref. [7], the ARPES measurements of Plate *et al.* for Tl-2201 were performed at very low energies [22] (tens of meV) and already capture the  $m^*$  renormalization. In LSCO, by contrast, the ARPES tight-binding fits to the dispersion [21] are carried out over a wider energy range—typically 0.5 eV—and therefore do not include the many-body renormalization. While some flattening of the LSCO dispersion is visible in ARPES (see Fig. 6 of Ref. [21]), it is not sufficiently well resolved to determine  $m^*/m$ . Instead, we turn to heat capacity measurements on Zn-doped LSCO [23,24], where the Zn doping has been used to suppress  $T_c$  to access the Sommerfeld coefficient in the low temperature limit. We model the Zn dopants as strong-scattering impurities with normal-state scattering rate  $\Gamma_N$ , and obtain a good fit to the doping-dependent Sommerfeld coefficient with  $\Gamma_N = 85$  K and  $m^*/m = 2.5$ , as shown in Fig. 4. This value of  $m^*/m$  has been used in all subsequent calculations on LSCO.

### B. Impurity potentials

We then describe the influence of the impurity in question in terms of a lattice impurity Hamiltonian  $H_{\text{imp}}$ , as described below. The impurity Hamiltonian consists of modifications of both the site energies and hopping matrix elements relative to the pure system, and is determined by a Wannier-based method for calculating impurity potentials [16] that has been used successfully, e.g., to accurately simulate strong disorder in superconducting materials [16,25–27]. In this method, two DFT calculations are carried out for each type of impurity: one of a  $3 \times 3 \times 1$  supercell containing a single impurity ( $\text{La}_{35}\text{SrCu}_{18}\text{O}_{72}$ ,  $\text{La}_{36}\text{Cu}_{18}\text{O}_{71}$ , or  $\text{Tl}_{35}\text{Ba}_{36}\text{Cu}_{19}\text{O}_{108}$ ); and a reference calculation for the corresponding pure system ( $\text{La}_4\text{Cu}_2\text{O}_8$  or  $\text{Tl}_4\text{Ba}_4\text{Cu}_2\text{O}_{12}$ ). For the (La,Sr) substitution and the O vacancy impurity potential in LSCO we have repeated the calculations for two different hole dopings, determined in each case by integrating the density of states (DOS) down from the top of the band to the Fermi level. In addition to the undoped calculations (in which no holes or electrons were

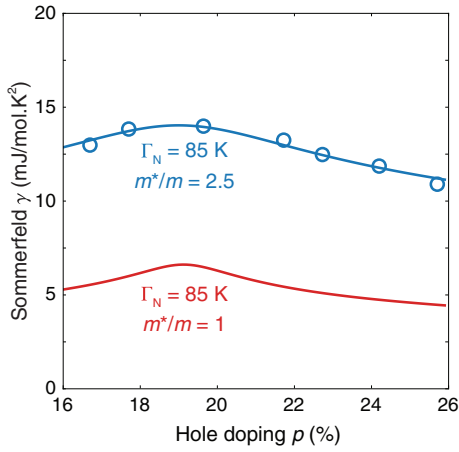


FIG. 4. Sommerfeld specific heat coefficient  $\gamma$  for Zn-doped LSCO. Experimental heat capacity data from Ref. [23] are fit using the ARPES-derived band structure [20] with scattering rate  $\Gamma_N$  and Fermi-liquid mass enhancement  $m^*/m$  as adjustable parameters, from which we determine  $m^*/m = 2.5$ . The unrenormalized Sommerfeld coefficient is shown below for comparison.

added, other than those added by the impurity itself), we have repeated the calculations with a hole doping ( $p_{\text{vH}}$ ) for which the van Hove singularity in the single impurity supercell lies at the Fermi level, and a second doping with 0.07 extra holes per Cu ( $p_{\text{vH}} + 7\%$ ). The reason for deriving the potentials at  $p_{\text{vH}}$  and  $p_{\text{vH}} + 7\%$  is that the enhanced density of states at the van Hove singularity has a strong effect on screening, making the impurity potentials substantially more local. More details of the first principles derivation of the impurity potential are given in Appendix A.

Each pair of DFT calculations is Wannier-projected onto a one-orbital lattice to obtain the supercell Hamiltonian for the  $i^{\text{th}}$  impurity type,  $H_{\text{supercell}}^i$ , and the reference Hamiltonian,  $H_0$ , respectively. The difference between the two tight-binding models then defines the Hamiltonian associated with the  $i^{\text{th}}$  impurity,

$$\begin{aligned} H_{\text{imp}}^i &\equiv (H_{\text{supercell}}^i - \mu^i \hat{N}^i) - (H_0 - \mu_0 \hat{N}) \\ &= \sum_{\mathbf{R}, \mathbf{R}', \sigma} \delta H_{\mathbf{R}\mathbf{R}'}^i c_{\mathbf{R}\sigma}^\dagger c_{\mathbf{R}'\sigma} \\ &\equiv \sum_{\mathbf{R}, \sigma} V_{\mathbf{R}}^i c_{\mathbf{R}, \sigma}^\dagger c_{\mathbf{R}\sigma} + \sum_{\mathbf{R} \neq \mathbf{R}', \sigma} \delta t_{\mathbf{R}\mathbf{R}'}^i c_{\mathbf{R}\sigma}^\dagger c_{\mathbf{R}'\sigma}, \end{aligned} \quad (1)$$

for which the Bloch-wave matrix elements are

$$\begin{aligned} V_{\mathbf{k}, \mathbf{k}'} &= \sum_{\mathbf{R}, \mathbf{R}'} \delta H_{\mathbf{R}\mathbf{R}'}^i e^{-i\mathbf{k}\cdot\mathbf{R}} e^{i\mathbf{k}'\cdot\mathbf{R}'} \\ &= \sum_{\mathbf{R}} V_{\mathbf{R}}^i e^{-i(\mathbf{k}-\mathbf{k}')\cdot\mathbf{R}} + \sum_{\mathbf{R} \neq \mathbf{R}'} \delta t_{\mathbf{R}\mathbf{R}'}^i e^{-i\mathbf{k}\cdot\mathbf{R}} e^{i\mathbf{k}'\cdot\mathbf{R}'}. \end{aligned} \quad (2)$$

Here  $\mu^i$  and  $\mu_0$  are the chemical potentials of the simulation with and without the impurity, respectively, determined directly from the DFT calculations via integration of the DOS. The 2D lattice vectors  $\mathbf{R}$  and  $\mathbf{R}'$  are measured in a coordinate system in which the impurity sits directly above (or below) the origin. Unlike the tight-binding Hamiltonian of a translationally invariant system, where all the site energies  $V_{\mathbf{R}}$  are

equivalent and the hopping integrals  $t_{\mathbf{R}\mathbf{R}'}$  can be classified into a small hierarchy of increasing-range terms (nearest neighbor, next-nearest neighbor, etc.), the impurity Hamiltonian lacks translational symmetry, with  $V_{\mathbf{R}}^i$  and  $\delta t_{\mathbf{R}\mathbf{R}'}^i$  falling off with distance from the impurity site. It is nevertheless useful to group equivalent terms together: this is illustrated in Fig. 3, and leads to the momentum-dependent form factors discussed in Appendix A and listed in Tables I–III. For the materials of interest here, defects can be classified into two types—site-centered and plaquette-centered—depending on where they sit with respect to the Cu atoms of the  $\text{CuO}_2$  plane. For the body-centered-tetragonal structures of LSCO and TI-2201 shown in Figs. 1 and 2, each out-of-plane defect in fact plays a dual role: site-centered with respect to one neighboring  $\text{CuO}_2$  plane and plaquette-centered with respect to the other. To illustrate the qualitative differences between the impurity potentials, the impurity matrix elements are plotted in Fig. 5 as  $|V(\mathbf{q})|^2$ , using the site energies from Tables I–III and Eq. (2). The Cu substituents in TI-2201, located well away from the  $\text{CuO}_2$  planes, have strong forward-scattering character, with  $|V(\mathbf{q})|^2$  peaked sharply near  $q = 0$  and its Umklapp replicas. By contrast, the impurity matrix elements in LSCO are more rounded, reflecting the much smaller separation of the defects from the  $\text{CuO}_2$  planes. The pointlike nature of the apical oxygen vacancy results in a significant constant contribution to  $|V(\mathbf{q})|^2$ .

Since DFT calculations on cuprates systematically overestimate the electronic bandwidth relative to the bandwidth measured in ARPES experiments, the DFT impurity potentials are first expressed in units of the DFT-derived nearest-neighbor hopping  $|t|$ , with the physically relevant value of  $|t|$  set later by ARPES, when including the impurity potentials in subsequent parts of the calculation. With these approximations in mind, a full, material-specific tight-binding model including disorder is obtained, to which we add a phenomenological  $d$ -wave pair potential to describe the superconducting state. The same procedure is followed systematically for all material systems considered.

As mentioned above, the dominant defects in LSCO are apical oxygen vacancies and the  $\text{Sr}^{2+}$  dopant ions that substitute for  $\text{La}^{3+}$ , thereby removing electrons from the conduction band. It is expected that each added Sr atom should dope one hole into the  $\text{CuO}_2$  planes, but the reality is more complicated. A discrepancy between Fermi volume and Sr content has been found in a number of ARPES studies [20,28,29], with the careful 3D Fermi-surface measurements of Ref. [29] revealing a Fermi volume equivalent to  $p = 0.32$ , significantly larger than the Sr concentration of their  $\text{La}_{1.78}\text{Sr}_{0.22}\text{CuO}_4$  sample,  $x = 0.22$ . A possible explanation of this effect is that in chemically tuning the Sr concentration, the equilibrium oxygen content is also changed. One way of taking this into account is to set the doping-dependent concentration of Sr defects,  $n_{\text{Sr}}$ , using the relation  $n_{\text{Sr}} = x = 0.69p$ . We also consider the conventional relation,  $n_{\text{Sr}} = p$ , and show that this does not significantly change our results. The relevant concentration of oxygen vacancies is more difficult to determine, but is known to be significant [30–32]. There are two inequivalent oxygen sites in LSCO: planar oxygen and apical oxygen. Structural refinements of x-ray diffraction data for LSCO in Ref. [31] reveal that the planar oxygen site is fully occupied

in well-annealed crystals (i.e., annealed at 500°C for 1 week, in 1 atm O<sub>2</sub>). By contrast, the apical oxygen is much less tightly bound, with the same sample containing apical oxygen vacancies at the  $n_{V_o} \approx 9\%$  level. Apical oxygen vacancies are also likely to be highly relevant to the molecular-beam epitaxy (MBE) thin films [3] of interest in the current study: their large lateral dimension makes diffusion times long, and their very high quality and crystallinity mean there are no grain boundaries or screw dislocations to provide an easy diffusion path perpendicular to the film. This is particularly apparent when the MBE films are patterned into narrow microbridges and annealed in ozone [3]—rapid diffusion of oxygen across the microbridges reduces their residual resistivity by up to a factor of 4 compared to the unpatterned cm<sup>2</sup> films [4]. With this in mind, our calculations of superfluid density for LSCO have been performed over a range of apical oxygen vacancy concentrations,  $4\% \leq n_{V_o} \leq 8\%$ .

The dominant defect in Tl-2201 is a consequence of its crystal growth. The high volatility of Tl<sub>2</sub>O<sub>3</sub> at the growth temperature leads to a deficit of Tl, which is replaced by an excess of Cu that substitutes onto 4% to 7.5% of Tl sites [11, 33–35]. Attempts to suppress the Cu–Tl substitution using high-pressure encapsulation [11] have been partially successful, but reveal that the excess Cu<sup>+</sup> plays a vital role in making Tl-2201 an overdoped cuprate. (Cu<sup>+</sup> has a valence of  $-2$  relative to Tl<sup>3+</sup>, making it an effective hole dopant. Interstitial O<sup>2-</sup> in the Tl<sub>2</sub>O<sub>2</sub> double layers is similarly effective at doping holes into the CuO<sub>2</sub> planes.) We have calculated the impurity potential of the Cu substituent and, assuming each Cu dopes two holes, have set its concentration to be  $n_{Cu} = p/2$ . Here  $n_{Cu}$  gives the concentration of Cu substituents as a fraction of the in-plane Cu and varies smoothly from 8% to 15% across the overdoped range. This is broadly in line with the direct measurements of Cu concentration cited above, remembering that there are two Tl sites for every in-plane Cu. To the extent that oxygen interstitials are present, we expect them to behave as dopants, and as scatterers, in much the same way as the Cu substituents, given their similar location and relative valence.

### C. Superconducting state

Within the Matsubara formalism, the Nambu space Green's function for a dirty superconductor can be written as [36]

$$\underline{G}(\mathbf{k}, i\omega_n) = -\frac{i\tilde{\omega}_{\mathbf{k},n}\tau_0 + \tilde{\Delta}_{\mathbf{k},n}\tau_1 + \xi_{\mathbf{k}}\tau_3}{\tilde{\omega}_{\mathbf{k},n}^2 + \tilde{\Delta}_{\mathbf{k},n}^2 + \xi_{\mathbf{k}}^2}, \quad (3)$$

where  $\xi_{\mathbf{k}}$  is the single-particle dispersion relative to the Fermi level and  $\tau_i$  are the Pauli particle–hole matrices. In anticipation of momentum-dependent scattering effects that arise from out-of-plane scatterers (and unlike the more common case of point scatterers) we include momentum dependence in the renormalized Matsubara frequencies,  $\tilde{\omega}_{\mathbf{k},n} \equiv \omega - \Sigma_0(\mathbf{k}, \omega_n)$ , and allow for explicit renormalization of the superconducting gap,  $\tilde{\Delta}_{\mathbf{k},n} \equiv \Delta_{\mathbf{k}} + \Sigma_1(\mathbf{k}, \omega_n)$ . We give the explicit forms of  $\tilde{\omega}_{\mathbf{k},n}$  and  $\tilde{\Delta}_{\mathbf{k},n}$  below. In principle, the band energy  $\xi_{\mathbf{k}}$  should also be self-consistently renormalized by the disorder, but this effect is generically weaker, indeed vanishing identically in the case of pointlike impurities in a particle–hole symmetric system. Furthermore, the real part of the self energy

$\Sigma_3 \equiv \tilde{\xi}_{\mathbf{k}} - \xi_{\mathbf{k}}$  is already incorporated into the ARPES-derived electronic structure employed here.

For a separable pairing interaction,  $V_0 d_{\mathbf{k}} d_{\mathbf{k}'}$ , the gap equation for a weak-coupling unconventional superconductor is [36]

$$\Delta_{\mathbf{k}} = \frac{2T}{N} \sum_{\omega_n > 0} \sum_{\mathbf{k}'} V_0 d_{\mathbf{k}} d_{\mathbf{k}'} \frac{\tilde{\Delta}_{\mathbf{k}',n}}{\tilde{\omega}_{\mathbf{k}',n}^2 + \tilde{\Delta}_{\mathbf{k}',n}^2 + \xi_{\mathbf{k}'}^2}, \quad (4)$$

where  $\Omega_c$  is a high-frequency cutoff, the  $\mathbf{k}'$  sum runs over the first Brillouin zone, and  $N$  is the number of sites in the lattice. For the tetragonal cuprates we are interested in, the  $d$ -wave eigenfunction takes the form

$$d_{\mathbf{k}} \propto [\cos(k_x a) - \cos(k_y a)], \quad (5)$$

where  $a$  is the in-plane lattice spacing, and  $d_{\mathbf{k}}$  is normalized such that  $\frac{1}{N} \sum_{\mathbf{k}} d_{\mathbf{k}}^2 = 1$ . The system thus condenses into the state  $\Delta_{\mathbf{k}} = \Delta_0 d_{\mathbf{k}}$  at all temperatures below  $T_c$ .

In addition to the weak-scattering *ab initio* potentials discussed above for the out-of-plane impurities, we also allow for a small density of in-plane strong scatterers, such as Cu vacancies. The combined effect of the strong and weak scatterers is shown diagrammatically in Fig. 6. Since the out-of-plane potentials are relatively weak, they can be treated in the Born approximation, a statement that we justify in more detail below. The in-plane strong scatterers are treated as pointlike unitarity scatterers in the  $t$ -matrix approximation. The out-of-plane defects generate potentials with significant spatial extent, leading in turn to strong momentum dependence in the matrix elements  $V_{\mathbf{k},\mathbf{k}'}$ . As a result, vertex corrections must be included in the calculation of two-particle properties such as superfluid density, resistivity and optical conductivity.

Including the extended nature of the dopant defects, the renormalization equations acquire a somewhat different form than is usual, but the self-energy contributions from the various impurity types are still additive [37]:

$$\tilde{\omega}_{\mathbf{k},n} = \omega_n + \frac{1}{N} \sum_{i, \mathbf{k}'} n_i |V_{\mathbf{k},\mathbf{k}'}^i|^2 \frac{\tilde{\omega}_{\mathbf{k},n}}{\tilde{\omega}_{\mathbf{k},n}^2 + \tilde{\Delta}_{\mathbf{k},n}^2 + \xi_{\mathbf{k}}^2} + \frac{\Gamma_N^U}{G_0}, \quad (6)$$

$$\tilde{\Delta}_{\mathbf{k},n} = \Delta_{\mathbf{k}} + \frac{1}{N} \sum_{i, \mathbf{k}'} n_i |V_{\mathbf{k},\mathbf{k}'}^i|^2 \frac{\tilde{\Delta}_{\mathbf{k},n}}{\tilde{\omega}_{\mathbf{k},n}^2 + \tilde{\Delta}_{\mathbf{k},n}^2 + \xi_{\mathbf{k}}^2}, \quad (7)$$

where

$$G_0 = \frac{1}{\pi N N_0} \sum_{\mathbf{k}} \frac{1}{2} \text{Tr}[\tau_0 \underline{G}(\mathbf{k}, i\omega_n)]; \quad (8)$$

$N_0$  is the single-spin density of states per unit cell, calculated self-consistently at the Fermi level;  $n_i = N_i/N$  is the concentration of the  $i$ th impurity; and  $\Gamma_N^U$  is the normal-state scattering rate associated with the strong-scattering impurities.

We note that the use of the Born approximation has been criticized as corresponding to an unphysical limit consisting of an infinite number of infinitely weak scatterers [4]. This is too narrow an interpretation. In fact, for dilute pointlike scatterers in effectively three dimensions, the Born approximation is justified whenever the quantity  $V_{\text{imp}} N_0$  is significantly less than one. (It is also common to parameterize the strength of a scatterer in terms of the cotangent of its scattering phase shift,

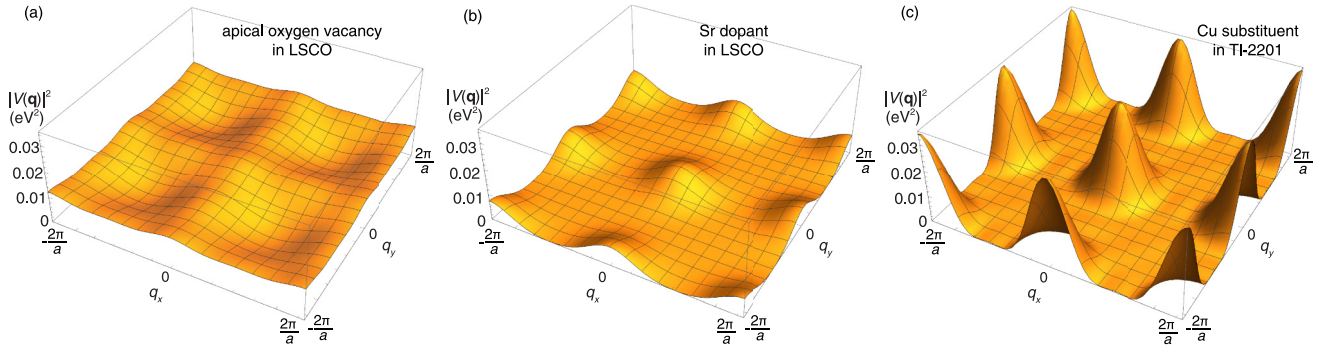


FIG. 5. Impurity matrix elements as a function of momentum transfer  $\mathbf{k} - \mathbf{k}' \equiv \mathbf{q} = (q_x, q_y)$  for: (a) the apical oxygen vacancy in LSCO; (b) the Sr dopant in LSCO; and (c) the Cu-Tl substitution in TI-2201. Matrix elements  $V(\mathbf{q})$  are obtained from Eq. (2), using the site-energies  $V_R^i$  from Tables I to III, respectively. (Hopping modifications are not included, but are in any case small.)

$c = \cot \delta = 1/(\pi V_{\text{imp}} N_0)$ : the Born-limit then corresponds to  $c$  significantly greater than 1.) In our previous work assuming pointlike impurities, we compared results for superfluid density calculated over a wide range of scattering phase shifts and showed that  $\rho_s(T)$  was qualitatively unchanged for  $c \geq 2$ , illustrating the broad applicability of the Born limit [7]. For the extended impurities considered here, the need to include vertex corrections to two-particle properties would make the full  $t$ -matrix approximation computationally expensive. There is, however, a simple test we can perform. The *ab initio* calculations show that our strongest scatterer, the near apical oxygen vacancy in LSCO, is essentially pointlike (i.e.,  $V_0 \gg V_2, V_4, \dots$ ), allowing it to be treated as a point scatterer in the  $t$ -matrix approximation, then compared to results obtained in the Born approximation. This test is carried out in Appendix D, with the conclusion that the Born approximation is well justified for all of our out-of-plane extended defects.

Another interesting aspect of extended impurities is that they give rise to momentum-dependent first-order corrections to the impurity self-energy, in contrast to the case of pointlike scatterers, for which the first-order correction is a constant that can be absorbed into the chemical potential. However, as discussed in Appendix A, the momentum dependence of the first-order self-energy arising from the hopping modifications

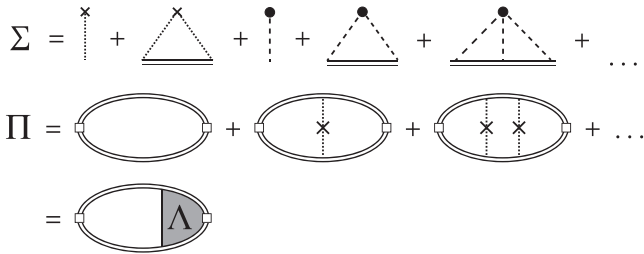


FIG. 6. Diagrammatic expansions of the disorder-averaged self energy  $\Sigma$  and polarization bubble  $\Pi$ , in the realistic disorder model. Circles denote pointlike strong impurities, which are treated in the  $t$ -matrix approximation. Crosses denote one type of weak extended scatterer, treated in the Born approximation. For simplicity the other species of weak scatterer are not shown, but appear as additive terms in the actual calculations. Only weak scatterers contribute to the vertex function  $\Lambda$ , and there are no crossing diagrams between different impurity types.

corresponds to the same form factors as in the normal state dispersion, such that these terms simply renormalize the band structure. Since we use tight-binding models derived from ARPES experiment, these effects are already incorporated into the dispersions adopted.

#### D. Transition temperatures $T_{c0}$ and $T_c$

For a clean system,  $\omega_n$  and  $\Delta_{\mathbf{k}}$  are unrenormalized and the gap equation is [36]

$$\Delta_{\mathbf{k}} = \frac{2T}{N} \sum_{\omega_n > 0} \sum_{\mathbf{k}'} V_0 d_{\mathbf{k}} d_{\mathbf{k}'} \frac{\Delta_{\mathbf{k}'}}{\omega_{\mathbf{k}'n}^2 + \Delta_{\mathbf{k}'}^2 + \xi_{\mathbf{k}'}^2}. \quad (9)$$

This allows the pairing strength  $V_0$  and cutoff  $\Omega_c$  to be parameterized in terms of a notional, clean-limit transition temperature  $T_{c0}$ , by carrying out the Matsubara sum in Eq. (9) at temperature  $T_{c0}$ , where  $\Delta_{\mathbf{k}}$  is vanishingly small and can be eliminated from the denominator:

$$\frac{1}{V_0} = \frac{2T_{c0}}{N} \sum_{\omega_n > 0} \sum_{\mathbf{k}} d_{\mathbf{k}}^2 \frac{1}{\omega_{\mathbf{k},n}^2 + \xi_{\mathbf{k}}^2}. \quad (10)$$

In the presence of disorder, the gap equation at  $T_c$  reduces to

$$\Delta_{\mathbf{k}} = \frac{2T_c}{N} \sum_{\omega_n > 0} \sum_{\mathbf{k}'} V_0 d_{\mathbf{k}} d_{\mathbf{k}'} \frac{\tilde{\Delta}_{\mathbf{k}'n}}{\tilde{\omega}_{\mathbf{k}'n}^2 + \xi_{\mathbf{k}'}^2}. \quad (11)$$

We now take  $T_c(p)$  to be given roughly by experiment, in each case assuming a parabolic form for the “superconducting dome.” Equations (10) and (11) can then be solved numerically in the presence of disorder to infer the value of  $T_{c0}$  required to produce a given  $T_c$ . The variation of  $T_{c0}$  with doping reflects the intrinsic physics of the cuprate pairing interaction, in particular its weakening on the overdoped side. We note that  $T_{c0}$  should be considered an upper bound on the clean-limit transition temperature, as we have not included pair-breaking effects arising from inelastic scattering, or fluctuation effects such as the Berezinskii–Kosterlitz–Thouless vortex-unbinding transition.

#### E. Superfluid density

The superfluid density is calculated within the Matsubara formalism by evaluating the electromagnetic response func-

tion in the static limit,  $\Omega \rightarrow 0$  [38,39]:

$$Q^{jj} = \frac{e^2 T}{N} \sum_{\omega_n > 0} \sum_{\mathbf{k}} \mathbf{v}_{\mathbf{k}}^i \text{Tr}[\underline{G}(\mathbf{k}, \omega_n) \Lambda^j \underline{G}(\mathbf{k}, \omega_n) - \tau_3 \underline{G}(\mathbf{k}, \omega_n) \Lambda^j \tau_3 \underline{G}(\mathbf{k}, \omega_n)], \quad (12)$$

$$\Lambda(\mathbf{k}, \omega_n) = \mathbf{v}_{\mathbf{k}}[\gamma_0(\mathbf{k}, \omega_n)\tau_0 + i\gamma_1(\mathbf{k}, \omega_n)\tau_1 + \gamma_3(\mathbf{k}, \omega_n)\tau_3], \quad (13)$$

where explicit expressions for the vertex components  $\gamma_n(\mathbf{k}, \omega_n)$  are given in Appendix E. The final result for the 2D superfluid density is

$$\rho_s^{2D}(T) = \mu_0 Q^{xx} = \frac{8\mu_0 e^2 T}{N} \sum_{\omega_n > 0} \sum_{\mathbf{k}} (\mathbf{v}_{\mathbf{k}}^j)^2 \frac{\tilde{\Delta}_{\mathbf{k},n}^2 \gamma_0(\mathbf{k}, \omega_n) - \tilde{\omega}_{\mathbf{k},n} \tilde{\Delta}_{\mathbf{k},n} \gamma_1(\mathbf{k}, \omega_n)}{(\tilde{\omega}_{\mathbf{k},n}^2 + \tilde{\Delta}_{\mathbf{k},n}^2 + \xi_{\mathbf{k}}^2)^2}. \quad (14)$$

The alert reader will note that we have presented formulas in which the  $\mathbf{k}$ -sum is performed over the whole Brillouin zone, rather than over the Fermi surface itself as in the previous work of Refs. [5–7]. This is done both because the kernel in the energy integration of Eq. (14) does not necessarily fall off rapidly enough near the Fermi surface, and because quantitative inaccuracies arise if calculations are carried out on the Fermi surface near those dopings where the van Hove singularity is close to the Fermi level. A comparison of the

where the first term and second terms are the diamagnetic and paramagnetic contributions, respectively. The group velocity along the  $j$  direction is  $\mathbf{v}_{\mathbf{k}}^j = \partial \xi_{\mathbf{k}} / \partial k^j$ , and  $\Lambda$  is the impurity-renormalized current vertex function,

two approaches is given in Appendix B, along with details of the implementation of the full-Brillouin-zone sum.

Sufficiently far from the van Hove singularity, where it is possible to linearize the spectrum  $\xi_{\mathbf{k}}$  and carry out the  $\xi$  integration, Eq. (14) can safely be recast as a Fermi surface average. Including vertex corrections, this leads to the following expression for  $\rho_s^{2D}$ :

$$\rho_s^{2D}(T) = 2\pi \mu_0 e^2 N_0 T \sum_{\omega_n > 0} \left\langle \left( \mathbf{v}_{\mathbf{k}}^j \right)^2 \frac{\tilde{\Delta}_{\mathbf{k},n}^2 \gamma_0(\mathbf{k}, \omega_n) - \tilde{\omega}_{\mathbf{k},n} \tilde{\Delta}_{\mathbf{k},n} \gamma_1(\mathbf{k}, \omega_n)}{(\tilde{\omega}_{\mathbf{k},n}^2 + \tilde{\Delta}_{\mathbf{k},n}^2)^{3/2}} \right\rangle_{\text{FS}_{\mathbf{k}}}, \quad (15)$$

which reduces to the familiar form for superfluid density used, e.g., in Refs. [5–7] in the limit  $\gamma_0 \rightarrow 1$  and  $\gamma_1 \rightarrow 0$  when the impurity potentials are pointlike.

### III. RESULTS

The *ab initio* calculations of impurity potentials are presented in Appendix A, in Tables I to III. DFT calculations were initially performed for LSCO, for the undoped supercells  $\text{La}_{35}\text{SrCu}_{18}\text{O}_{72}$  and  $\text{La}_{36}\text{Cu}_{18}\text{O}_{71}$ . In LSCO, the density of states has a particularly strong doping dependence: at a hole doping of around 19%, the Fermi surface undergoes a Lifshitz transition and a van Hove singularity passes through the Fermi level. To understand how this influences screening, two further sets of calculations were carried out: one at  $p = p_{\text{vH}}$ , with electron count adjusted to place the van Hove singularity at the Fermi level; and an even more overdoped calculation at  $p_{\text{vH}} + 7\%$ . Proximity to the van Hove singularity does indeed have a significant effect on the potentials, particularly for the near apical oxygen vacancy  $V_{\text{O}}^{\text{near}}$ . In Table I, we see that for undoped  $\text{La}_{36}\text{Cu}_{18}\text{O}_{71}$ , the impurity potential for  $V_{\text{O}}^{\text{near}}$  is rather extended: the on-site energy  $V_0$  is comparable in magnitude to the combined energies of the four nearest-neighbor sites ( $4 \times V_2$ ). This changes markedly at  $p_{\text{vH}}$ :  $V_{\text{O}}^{\text{near}}$  becomes essentially pointlike, with  $V_0 \gg V_2, V_4$ . As expected, the screening effect diminishes somewhat beyond the van Hove singularity: at  $p_{\text{vH}} + 7\%$  the on-site energy  $V_0$  increases by 6%, while the nearest-neighbor energy  $V_2$  dou-

bles, leading to a slightly more extended impurity potential. Proximity to the van Hove singularity also has a systematic effect on the screening of the potential of the Sr dopant, as seen in Table II. However, the changes are not as strong, nor as important: unlike  $V_{\text{O}}^{\text{near}}$ , the  $\text{Sr}^{\text{near}}$  defect is plaquette-centered, so its impurity potential is inherently extended. Results for the Cu defect in Tl-2201 are presented in Table III. Here DFT calculations were only carried out for the undoped  $\text{Tl}_{35}\text{Ba}_{36}\text{Cu}_{19}\text{O}_{108}$  supercell: there is no Lifshitz transition in Tl-2201 in the relevant doping range and, as discussed in Sec. II A, the Cu–Tl substitution already has a hole-doping effect.

As mentioned above, the spatially extended nature of the realistic disorder model gives rise to impurity matrix elements  $V_{\mathbf{k},\mathbf{k}'}$  with very strong momentum dependence. This, combined with anisotropic electronic structure, leads to elastic scattering rates that vary strongly around the Fermi surface, something that is a well-established part of cuprate phenomenology [21,22,40–49]. Recognizing that our calculation includes only disorder contributions, and not inelastic scattering, the normal-state elastic scattering rate  $\Gamma_N(\phi)$  is plotted in Figs. 7(a) and 7(b), for LSCO and Tl-2201.  $\Gamma_N(\phi)$  is defined to be the imaginary part of the  $\tau_0$  self energy above  $T_c$ , evaluated on the Fermi surface, at angle  $\phi$ . The scattering rate has significant angle dependence in both materials, being strongest in both cases at the antinodes, with minima along the zone diagonals, in qualitative agreement with ARPES [21,22,42,45,47,48] and transport [40,46,49]

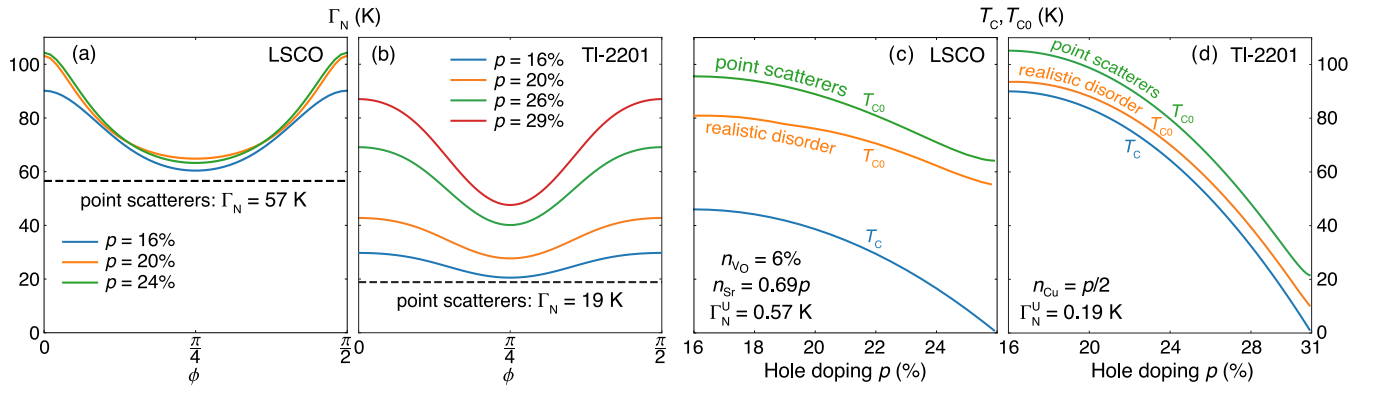


FIG. 7. Comparison of point-scattering and realistic disorder models in LSCO and TI-2201. (a, b) Normal-state elastic scattering rate  $\Gamma_N$  as a function of angle  $\phi$ , measured from the zone axes. Dashed lines indicate the values of  $\Gamma_N$  used in the point-scattering models of Refs. [5–7]. (c, d) Clean-limit transition temperatures  $T_{c0}(p)$  parametrize the pairing strength required to produce the parabolic “superconducting domes”  $T_c(p)$  of LSCO and TI-2201. Disorder parameters for the LSCO and TI-2201 plots are as shown in panels (c) and (d), respectively.

experiments on various cuprate materials. In LSCO, the calculated  $\Gamma_N(\phi)$  has very little doping dependence, but in TI-2201, both the magnitude and angle dependence of  $\Gamma_N(\phi)$  increase significantly with hole doping.

ARPES experiments do not, in general, have sufficient resolution to allow a quantitative comparison with our calculated  $\Gamma_N(\phi)$ . Clearer insights come from angle-dependent magnetoresistance (ADMR), with  $\Gamma(\phi)$  accessible through detailed, Boltzmann-transport fits to the ADMR data. We are not aware of ADMR measurements on LSCO, but results have recently been reported for Nd-doped LSCO [49], in which the Nd dopants shift the Lifshitz transition upwards from  $p = 19\%$  to  $p = 24\%$ . By carrying out these measurements at multiple temperatures, elastic and inelastic contributions to  $\Gamma(\phi)$  have been separated. The results from Ref. [49] reveal an elastic scattering rate in Nd-LSCO qualitatively similar to our calculations, with minima along the nodal directions and maxima at the antinodes. Converting the ADMR values to temperature units, and remembering that the experimentally accessible scattering rate is  $2\Gamma_N(\phi)$ , the nodal minimum in Nd-LSCO corresponds to  $\Gamma_{ADMR}^{\text{elastic}}(\phi=45^\circ) = 35$  K. This is somewhat smaller than our calculated nodal minimum for LSCO in Fig. 7(a),  $\Gamma_N(\phi=45^\circ) \approx 65$  K, which assumes a concentration of apical oxygen vacancies  $n_{VO} = 6\%$ . We have also carried out calculations for  $n_{VO} = 4\%$  and find  $\Gamma_N(\phi=45^\circ) \approx 43$  K. This is significantly closer to the ADMR value, and indicates that a lower concentration of apical oxygen vacancies in the Nd-LSCO crystals could easily account for the difference. The antinodal scattering rate is another matter, however. In our calculations, the angular variation in  $\Gamma_N$  is slightly less than a factor of 2. The scattering rate inferred from ADMR varies by a factor 8 around the Fermi surface, reaching an antinodal maximum of 275 K in  $\Gamma_N$  units. We suspect that this discrepancy is an artifact of the Fermi-surface-based Boltzmann-transport approach used to model the ADMR data, which breaks down in the vicinity of a van Hove singularity for the reasons we give in Appendix B, requiring full-B Brillouin-zone  $\mathbf{k}$ -sum methods instead.

For overdoped TI-2201 ( $T_c = 15$  K), the detailed interpretation of ADMR data in Ref. [46] found an elastic scattering

rate corresponding to  $\Gamma_N = 20$  K, with no significant variation around the Fermi surface. This is close to what we calculate for TI-2201 at optimal doping, but not with the doping dependence we show in Fig. 7(b). A detailed investigation of the behavior of the normal state scattering rate is beyond the scope of the current work, but it is worth emphasizing two key differences between LSCO and TI-2201 that must play an important role in any attempt to do so. First, LSCO passes through a Lifshitz transition in the overdoped superconducting range, with the van Hove singularity significantly enhancing its antinodal density of states; the TI-2201 Fermi surface is far from the vHS, with a relatively isotropic density of states. And second, the elastic scatterers in TI-2201 are located much further from the  $\text{CuO}_2$  planes than in LSCO, with concomitantly softer and longer-range potentials, as can be seen in Tables I to III.

For comparison purposes, the values of  $\Gamma_N$  used in the point-scattering models of Refs. [5–7] are also shown in Figs. 7(a) and 7(b), and correspond quite closely to the minima of  $\Gamma_N(\phi)$  in LSCO and TI-2201. This leads to an important insight—when defects are spatially extended, significantly higher scattering rates can be tolerated, particularly near the antinodes. This is because extended defects are inherently forward scattering. Near the antinodes, forward scattering couples states for which the  $d$ -wave gap has the same sign, a process akin to Anderson’s theorem [50], and harmless to superconductivity [51,52]. This can further be seen in Figs. 7(c) and 7(d), where plots of clean-limit transition temperature,  $T_{c0}(p)$ , show the pairing strength needed to produce the parabolic “superconducting domes” of LSCO and TI-2201. We see that the required pairing strength is somewhat lower than for the point scatterers of Refs. [5–7], despite the larger average scattering rate in Figs. 7(a) and 7(b). For LSCO this is particularly welcome, as the large values of  $T_{c0}(p)$  needed in Refs. [5–7] were a distinct weakness of the point-scattering approach. It is intriguing that this suggests an intrinsic pairing scale of about 80 K in doped  $\text{La}_2\text{CuO}_4$ , slightly higher than the 70 K of superoverdoped  $\text{Ba}_3\text{Cu}_2\text{O}_{4-\delta}$  [53]. As expected, in the TI-2201 system, the  $T_c$  suppression by disorder is considerably weaker than in LSCO.



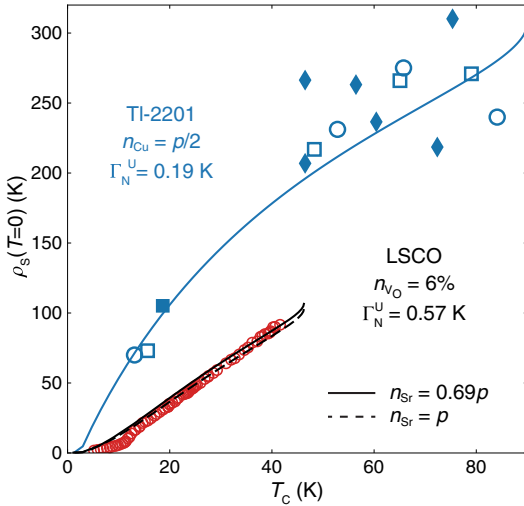


FIG. 8. Zero-temperature superfluid density as a function of transition temperature  $T_c$  for LSCO and TI-2201. Disorder parameters are as shown including, for LSCO, two different doping dependencies of Sr concentration,  $n_{\text{Sr}}(p)$ . LSCO data:  $\circ$  MBE thin-film mutual inductance [3]. TI-2201 data:  $\blacksquare$  single-crystal microwave [54];  $\blacklozenge$  single-crystal  $\mu\text{SR}$  [55];  $\circ$ ,  $\square$  polycrystalline  $\mu\text{SR}$  [56,57].

Figure 8 shows zero-temperature superfluid density as a function of transition temperature  $T_c$  in LSCO and TI-2201 (and compares with experimental data from Refs. [54–57]). The *ab initio* calculations do a remarkably good job of capturing the experimental behavior, particularly in the case of TI-2201, where the sole assumption is that the concentration of out-of-plane scatterers is given by  $n_{\text{Cu}} = p/2$ . In LSCO, the data of Ref. [3] are well described by a calculation based on 6% apical oxygen vacancies. In Appendix C, the effect of varying the concentration of Sr and  $V_{\text{O}}$  defects in LSCO is explored in more detail. The pointlike potential of the apical oxygen vacancies has a significant pair-breaking effect; the spatially extended potential of the Sr defects renders them fairly benign to the superfluid density, as can be seen in Fig. 8 by comparing the traces for  $n_{\text{Sr}} = p$  and  $n_{\text{Sr}} = 0.69p$ .

Figure 9 shows the temperature dependence of  $\rho_s$  for the same *ab initio* potentials as in Fig. 8, along with the experimental data for LSCO from Ref. [3]. As expected from Refs. [5,7], the temperature dependence is remarkably linear down to temperatures of order 1 K, at which point the materials enter a gapless regime indicative of a narrow impurity band, controlled in our model by the presence of a small density of unitarity scatterers. In general, the agreement with the data of Ref. [3] shown in Fig. 9(a) is excellent over the entire temperature and doping range, with the exception of deviations near  $T_c$ , which are discussed in Ref. [5]; and for the very lowest  $T_c$  sample, which was discussed in detail in Ref. [10]. We do not currently understand the latter discrepancy: the disorder-averaged theory suggests that significant curvature will occur in  $\rho_s(T)$  at the lowest temperatures, but this is not visible in the experimental data on that sample. It may be that the very low  $T_c$  samples are more inhomogeneous and have such low superfluid density that they are indeed dominated by phase fluctuations rather than Bogoliubov quasiparticles.

## IV. DISCUSSION

### A. Critical assessment of approach

Here we present what we regard as the strong and weak points of the analysis we have presented. A major advantage of our approach, a simple extension of “dirty  $d$ -wave theory,” is certainly its simplicity: one can work in the superconducting state with a theory of well-defined quasiparticles and calculate essentially any observables. We have now updated this theory to start from *ab initio* calculations of the relevant impurity strengths in the systems of interest and shown that the results continue to agree well with recent superfluid density experiments; the number of free parameters not precisely constrained by experimental data or the *ab initio* calculations has thus been significantly reduced. Furthermore, we show in Appendix B that the van Hove singularity, which naively could give rise to anomalies in such a theory at dopings when it approaches the Fermi level, is in fact rather benign when properly treated using momentum-sum methods rather than Fermi-surface averages.

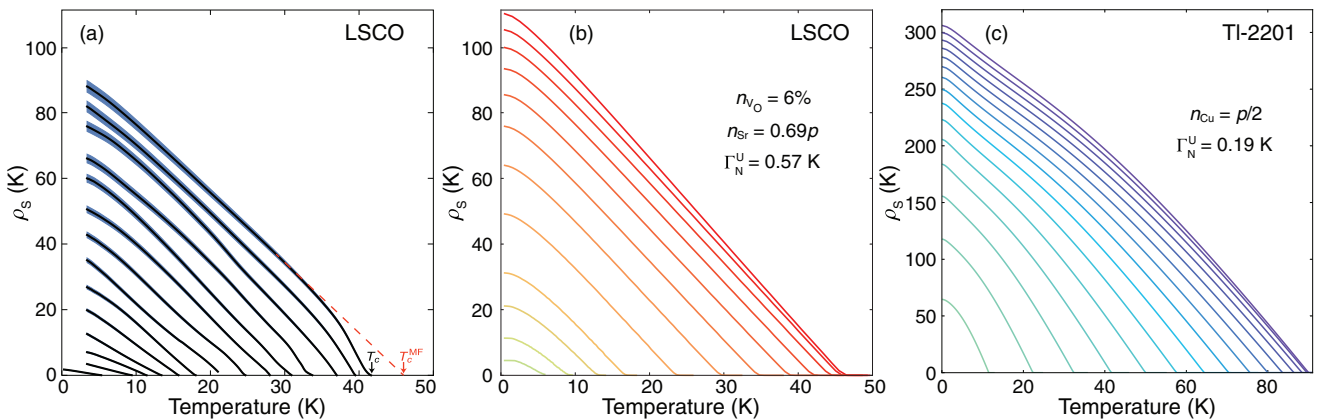


FIG. 9. Temperature-dependent superfluid density of overdoped LSCO and TI-2201. (a) Superfluid density data for LSCO from Ref. [3], with shading indicating the stated 2% experimental uncertainty. The dashed line indicates the construction used to estimate the corresponding mean-field transition temperature  $T_c^{\text{MF}}$ . (b, c) Superfluid density for LSCO and TI-2201 calculated in the realistic disorder model, for the disorder parameters shown, as doping (and therefore  $T_c$ ) are varied.

Nevertheless, the present approach could be improved in several ways. First, as we have noted above, one could study the out-of-plane dopant impurities within the  $t$ -matrix rather than Born approximation. This would be more accurate, but makes calculation of the corresponding vertex corrections to two-particle properties significantly more expensive. We have argued that, for the calculated impurity potential values,  $t$ -matrix and Born approximation calculations must give essentially identical results.

A complete theory would also account explicitly for the doping effect of Sr/La, Cu/Tl, and O vacancy impurities on the electronic structure. This approach, i.e., assuming that every impurity dopes the system, was adopted, e.g., in Ref. [58]. While appealing in its simplicity, it does not reflect the complexity of different impurities and dopants in the cuprates. We have therefore chosen to calculate the *ab initio* scattering potentials directly, and have incorporated the changes in electronic structure by adopting the ARPES-derived tight binding models interpolated across the doping range. A direct implementation of *ab initio* doping is beyond the scope of the present theory, but it might be feasible in some future implementation of DFT+DMFT or similar realistic theories of electronic structure incorporating correlations.

In addition, we have performed our calculations of superconducting-state observables on a two-dimensional lattice of Cu  $3d_{x^2-y^2}$  orbitals. We thereby miss explicit inclusion of O and other out-of-plane ionic degrees of freedom in the tight-binding electronic structure, except insofar as they contribute to the single hybridized Cu–O band near the Fermi level. In some cuprates, 3D effects can be important at the level of electronic structure, particularly in tight-binding descriptions of the CuO<sub>2</sub> plane near van Hove singularities, as shown in Ref. [59].

Finally, we note that as in previous work, we have assumed that the pairing interaction binding electrons into a  $d$ -wave state can be adequately described in the weak-coupling limit, by a separable pairing interaction, the strength of which is parameterized by an assumed  $T_{c0}(p)$ , chosen to reproduce the experimental superconducting phase diagram. In a complete theory, the weakening of the clean-limit pairing interaction with increasing doping in the overdoped regime should be calculated from microscopics as well. For example, one might expect the doping and disorder to modify the particle–hole susceptibility as one moves across the phase diagram, thereby modifying the underlying spin-fluctuation pairing strength [60]. Including simple models of the disorder self-energy in such theories has already been attempted [61]. It will certainly be worthwhile to explore combining these approaches with our microscopic, material-specific disorder models.

### B. Electronic inhomogeneity

In this paper, we have explored the predictions of a simple theory describing a homogeneously disordered system, i.e., we have assumed that defects are distributed randomly and perturb the otherwise homogeneous system only weakly. This allows the application of a conventional disorder-averaged “effective medium” approach, which can be considered a simple generalization of the successful “dirty  $d$ -wave” theory

applied earlier to cuprates. In such a picture, the temperature dependence of thermodynamic and transport properties in the superconducting state is dominated by Bogoliubov quasiparticles. Furthermore, the disappearance of superconductivity on the overdoped side of the dome must be considered to be a consequence of a combination of a weakening of the  $d$ -wave pairing interaction and disorder (see, e.g., Ref. [61]).

On the other hand, there are several studies of cuprates generally, and of LSCO in particular, which propose a very different picture of the overdoped systems, one in which larger-scale inhomogeneity is *intrinsic* to the materials, and therefore  $T_c$  is determined not by uniform suppression of the gap, but by the destruction of the Josephson coupling between grains by phase fluctuations. For example, a recent study [62] considering several measures of superconductivity on an overdoped LSCO crystal found strong nanoscale inhomogeneity in STM and an onset of diamagnetism many degrees above the onset of zero resistance, consistent with a theory of granular superconductivity by Spivak *et al.* [63]. There is evidence from STM on many Bi-based cuprates of substantial inhomogeneity of local gaps and other properties of these samples [64,65].

Nevertheless, thermodynamic measurements tend to infer much narrower spatial distributions of superconducting properties in the overdoped regions than STM, particularly in the cleaner YBCO material [66,67] (overdoped with Ca). Even in LSCO, sample quality varies dramatically between crystals and thin films of various types, and there is to our knowledge no evidence for gross inhomogeneity in the epitaxially grown films of Ref. [3] with which we compare here. Recently, a careful study of Ca substitution concluded that reducing the disorder strength can dramatically extend the  $T_c$  dome of LSCO [68], supporting the notion that the destruction of superconductivity depends strongly on the scattering potentials of the dopants, as assumed here. From the theoretical standpoint, while it has been proposed that highly disordered  $d$ -wave superconductors can exhibit responses consistent with a granular picture [58] a recent study searching for this effect found no significant self-organization of regions of well-defined phase [69].

It therefore seems likely that, while granular, phase-fluctuation-dominated behavior may indeed exist in some overdoped samples, it is not *intrinsic* to cuprates, but rather due to chemical inhomogeneities that arise naturally in the growth process of some samples of some materials. In this case, the description of the somewhat idealized disorder-averaged dirty  $d$ -wave theory may indeed prove adequate for most of the overdoped phase diagram, until the falling superfluid density induces strong phase fluctuations [70] that may overcome the quasiparticle responses for some observables in samples with very small  $T_c$ . Furthermore, it seems to us unlikely that a theory of weakly Josephson-coupled grains can explain the superfluid density, optical conductivity, specific heat and thermal conductivity at the same semiquantitative level put forward here and in Refs. [5–7].

## V. CONCLUSIONS

As discussed in the Introduction, we have started from the point of view that the experimental data on the overdoped side of the cuprate phase diagram can be explained within the

Landau-BCS paradigm, provided the details of the disorder present as a result of the doping process are properly accounted for, with appropriate Fermi liquid renormalizations of quasiparticle masses fixed by experiment. Within this scheme, the dopant disorder is taken to be weak enough to apply the Born approximation for impurity scattering. A small concentration of strong, pointlike scatterers, representing in-plane defects such as Cu vacancies, has also been included, to reproduce the small gapless impurity band observed at the lowest temperatures. The impurity potentials themselves have now been calculated from first principles, scaled only by an overall bandwidth renormalization, yielding a tractable theory within which any superconducting state observable can be calculated. We have shown here that for the two cuprates that can be easily overdoped, these simple conventional procedures produce results consistent with the “anomalous” behavior of the superfluid density that has been observed.

### ACKNOWLEDGMENTS

We are grateful for useful discussions with M. P. Allan, J. S. Dodge, S. A. Kivelson, T. A. Maier, D. J. Scalapino, J. E. Sonier, and J. M. Tranquada. D.M.B. acknowledges financial support from the Natural Science and Engineering Research Council of Canada. P.J.H. acknowledges support from NSF-DMR-1849751. V.M. was supported by NSFC Grant No. 11674278 and by the priority program of the Chinese Academy of Sciences Grant No. XDB28000000. The first-principles calculations in this work (X.K. and T.B.) were conducted at the Center for Nanophase Materials Sciences, a U.S. Department of Energy Office of Science User Facility, operated at Oak Ridge National Laboratory. We used resources of the Compute and Data Environment for Science (CADES) at the Oak Ridge National Laboratory, which is supported by the Office of Science of the U.S. Department of Energy under Contract No. DE-AC05-00OR22725. In addition, this research used resources of the National Energy Research Scientific Computing Center (NERSC), a U.S. Department of Energy Office of Science User Facility located at Lawrence Berkeley National Laboratory, operated under Contract No. DE-AC02-05CH11231 using NERSC award BES-ERCAP0020403.

### APPENDIX A: IMPURITY POTENTIALS

As summarized above, the calculation of the impurity potential associated with a given defect requires two DFT calculations to be carried out: one for a supercell containing a single impurity; and a reference calculation of the corresponding pure system. For these calculations we employed the Vienna *ab initio* simulation package (VASP) [71] with the generalized gradient approximation of Perdew, Burke, and Ernzerhof [72] and a plane-wave energy cutoff of 650 eV. For the reference systems we used the conventional orthogonal  $\text{La}_4\text{Cu}_2\text{O}_8$  and  $\text{Tl}_4\text{Ba}_4\text{Cu}_2\text{O}_{12}$  cells with structural parameters corresponding to the Inorganic Crystal Structure Database (ICSD) entries 41643 and 65326, respectively [73]. The  $k$ -grids were taken to be  $21 \times 21 \times 6$  and  $7 \times 7 \times 6$  for the  $\text{La}_4\text{Cu}_2\text{O}_8$  normal cells and supercells, respectively. For the  $\text{Tl}_4\text{Ba}_4\text{Cu}_2\text{O}_{12}$  normal cells and supercells, the  $k$ -grids

were taken to be  $12 \times 12 \times 2$  and  $4 \times 4 \times 2$ , respectively. To derive the impurity potentials for the (La,Sr) substitution and the O vacancy impurity potential in LSCO with the additional hole dopings we proceeded as follows. We adjusted the VASP parameter NELECT in such a way that the van Hove singularity in the supercell lies at the Fermi energy. For the  $\text{La}_{35}\text{SrCu}_{18}\text{O}_{72}$  supercell this required us to subtract 0.11 electrons per Cu from the default value of NELECT. For the  $\text{La}_{36}\text{Cu}_{18}\text{O}_{71}$  supercell this number was 0.26 electrons per Cu instead. This difference can be roughly understood from the fact that a Sr dopes 1 hole, and an O vacancy removes 2 holes:  $0.11 + 1/18 \approx 0.26 - 2/18$ . We note that for these impurity potential derivations, NELECT was adjusted both in the single impurity supercell, and the reference system ( $\text{La}_4\text{Cu}_2\text{O}_8$  in this case) by the same number of holes per Cu. Adjusting the NELECT parameter adds a constant positive/negative background potential that essentially mimics the many positively/negatively charged Sr and O vacancy defects that are distributed throughout the sample, *not* the single, isolated impurity for which the *ab initio* potential is being calculated. In the single-impurity approach taken in our study, these background corrections are the most straightforward approximation to take into account the potentials induced by the nonzero density of dopants and vacancies present in sample. In addition to the van Hove hole doping  $p_{\text{vH}}$ , we also derived the impurity potentials of the (La,Sr) substitution and the O vacancy in LSCO for the hole doping  $p_{\text{vH}} + 7\%$  in which 0.07 extra holes were doped per Cu. In total 11 DFT calculations were performed to derive the impurity potentials of the (La,Sr) substitution and the O vacancy in LSCO for various hole dopings. For the undoped impurity potentials we simulated  $\text{La}_4\text{Cu}_2\text{O}_8$ ,  $\text{La}_{35}\text{SrCu}_{18}\text{O}_{72}$ , and  $\text{La}_{36}\text{Cu}_{18}\text{O}_{71}$  with the default value of NELECT. For the (La,Sr) potential at  $p_{\text{vH}}$  and  $p_{\text{vH}} + 7\%$  we simulated  $\text{La}_4\text{Cu}_2\text{O}_8$  and  $\text{La}_{35}\text{SrCu}_{18}\text{O}_{72}$  in which 0.11 and 0.18 electrons were removed from the default value of NELECT. For the O vacancy potential at  $p_{\text{vH}}$  and  $p_{\text{vH}} + 7\%$  we simulated  $\text{La}_4\text{Cu}_2\text{O}_8$  and  $\text{La}_{35}\text{SrCu}_{18}\text{O}_{72}$  in which 0.26 and 0.33 electrons we removed from the default value of NELECT. We emphasize again that in addition to the explicit removal of electrons, the impurities themselves also dope holes and electrons: a Sr dopes 1 hole, and an O vacancy dopes 2 electrons.

We note that the impurity potential needs to be partitioned from its super-images. To this end we use the partitioning scheme detailed in the supplement of Ref. [16]. The Wannier-function-based Hamiltonian has been derived using the Wannier90 software [74]. Specifically, we projected  $\text{Cu-}d_{x^2-y^2}$  orbitals on the bands within low-energy windows. These low-energy windows were taken to be  $[-4.5, 2.5]$  eV for the  $\text{La}_4\text{Cu}_2\text{O}_8$  normal cell and  $\text{La}_{35}\text{SrCu}_{18}\text{O}_{72}$  supercell;  $[-4.6, 2.3]$  eV for the  $\text{La}_{36}\text{Cu}_{18}\text{O}_{71}$  supercell; and  $[-3, 2.8]$  eV for the  $\text{Tl}_4\text{Ba}_4\text{Cu}_2\text{O}_{12}$  normal cell and the  $\text{Tl}_{35}\text{Ba}_{36}\text{Cu}_{19}\text{O}_{108}$  supercell. To obtain projected Wannier functions we set `num_iter` = 0. Due to the large number of orbitals in the supercells, the disentanglement procedure became unstable. Therefore, we set `dis_num_iter` = 0. As a result, the Wannier bands in some parts of  $k$ -space were shifted downwards in energy relative to the DFT bands (see Fig. 10). The most important consideration for the purposes of calculating impurity potentials is that the underlying Wannier

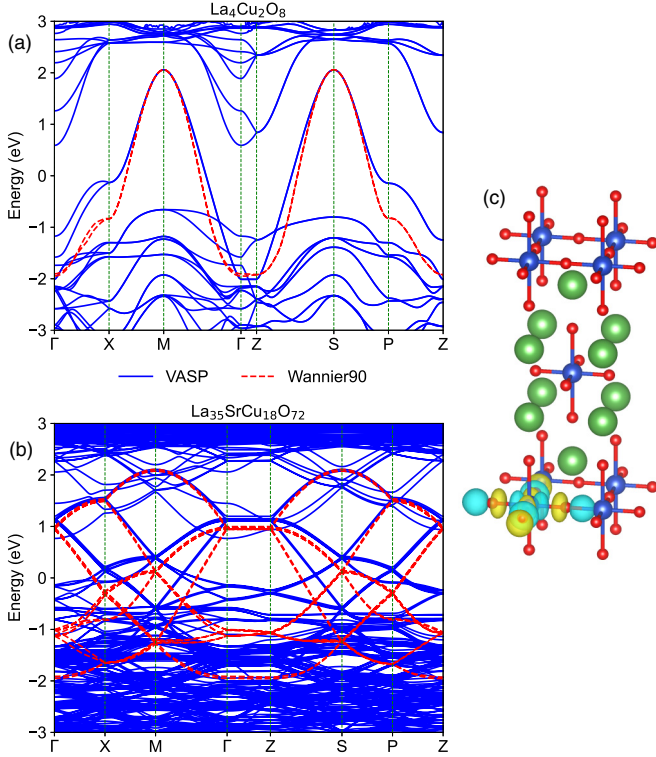


FIG. 10. Comparison of the VASP DFT band structure (solid lines) with the Wannierized bands (dashed lines) used to generate the tight-binding impurity potentials, for (a) the undoped  $\text{La}_4\text{Cu}_2\text{O}_8$  normal cell and (b) the  $\text{La}_{35}\text{SrCu}_{18}\text{O}_{72}$  supercell, containing one Sr dopant. The high-symmetry points are given by:  $\Gamma = (0, 0, 0)$ ,  $X = (\frac{1}{2}, 0, 0)$ ,  $M = (\frac{1}{2}, \frac{1}{2}, 0)$ ,  $Z = (0, 0, \frac{1}{2})$ ,  $S = (\frac{1}{2}, \frac{1}{2}, \frac{1}{2})$ ,  $P = (\frac{1}{2}, 0, \frac{1}{2})$ , and  $Z = (0, 0, \frac{1}{2})$ . For the  $\text{La}_4\text{Cu}_2\text{O}_8$  and  $\text{La}_{35}\text{SrCu}_{18}\text{O}_{72}$  bands these are expressed in the reciprocal basis vectors of the orthogonal  $\text{La}_4\text{Cu}_2\text{O}_8$  and  $\text{La}_{35}\text{SrCu}_{18}\text{O}_{72}$  unit cells, respectively. (c) The Wannier function, displaying well-localized Cu  $d_{x^2-y^2}/\text{O } p_{x,y}$  antibonding character. We emphasize that the Wannier bands are only used in the determination of the impurity potentials: the empirical ARPES band structure is the basis for all other calculations.

functions have well-localized Cu  $d_{x^2-y^2}/\text{O } p_{x,y}$  antibonding character, as can be seen in Fig. 10(c). In any case, some of the mismatch is canceled because the impurity potential is the difference between the single impurity supercell Hamiltonian and the reference Hamiltonian, as shown in Eq. (1).

Results for the *ab initio* impurity-potential calculations are presented in Tables I–III, with numerical values of the real-space matrix elements  $\delta H_{\mathbf{R}\mathbf{R}'}^i = V_{\mathbf{R}}^i \delta_{\mathbf{R},\mathbf{R}'}$  and  $\delta t_{\mathbf{R}\mathbf{R}'}^i$  given for representative choices of  $\mathbf{R}$  and  $\mathbf{R}'$ , in units of the DFT-derived nearest-neighbor hopping  $|t|$ . As shown in Fig. 3, it is useful to group together terms that are equivalent by symmetry. Transforming to momentum space, as shown in Eq. (2), the grouping of like terms leads to a set of form factors that enter the matrix elements  $V_{\mathbf{k},\mathbf{k}'}^i$ . For the site energies these are

$$f(\mathbf{k}, \mathbf{k}') = f(\mathbf{q}) = \sum_{\{\text{equiv. } \mathbf{R}\}} e^{i(\mathbf{k}-\mathbf{k}')\cdot\mathbf{R}} = \sum_{\{\text{equiv. } \mathbf{R}\}} e^{i\mathbf{q}\cdot\mathbf{R}}, \quad (\text{A1})$$

and for the hopping modifications

$$f(\mathbf{k}, \mathbf{k}') = \sum_{\{\text{equiv. } (\mathbf{R}, \mathbf{R}')\}} e^{i\mathbf{k}\cdot\mathbf{R}} e^{-i\mathbf{k}'\cdot\mathbf{R}'}, \quad (\text{A2})$$

where in each case the phase factors are summed over the set of equivalent lattice vectors  $\mathbf{R}$  or pairs of lattice vector  $(\mathbf{R}, \mathbf{R}')$ . By using a 2D coordinate system in which the impurity sits directly above (or below) the origin, we obtain form factors that are purely real. These are listed beside their corresponding impurity terms in Tables I–III, along with the form factor evaluated in the limit  $\mathbf{k} = \mathbf{k}'$  (i.e.,  $\mathbf{q} = 0$ ), as this is the form in which it enters the first-order self energy. In this limit, the site-energy form factors are constants that can be absorbed into the chemical potential. Interestingly, in the  $\mathbf{q} = 0$  limit, the form factors derived from the hopping modifications take on precisely the form of the band dispersions they modify, meaning that they can be directly absorbed into a renormalization of the hopping integrals. In this sense, we have taken the first-order self energy into account from the outset, since we base our energy dispersions on ARPES-derived tight-binding parametrizations.

To account for the doping dependence of the *ab initio* impurity potentials in LSCO, linear interpolation is used between  $p_{\text{vH}}$  and  $p_{\text{vH}} + 7\%$ . The overdoped regime is sufficiently far removed from the undoped compounds that interpolation does not make sense below  $p_{\text{vH}}$ ; constant extrapolation of the  $p_{\text{vH}}$  values is used instead.

## APPENDIX B: MOMENTUM SUMS AND THE VAN HOVE SINGULARITY

In calculations such as those carried out here, Brillouin-zone momentum sums are typically converted to Fermi-surface integrals, by linearizing the dispersion  $\xi_{\mathbf{k}}$  in the vicinity of the Fermi surface: i.e.,  $\xi_{\mathbf{k}} \rightarrow \hbar|\mathbf{v}_{F,k_{\parallel}}|\delta k_{\perp}$ . In a 2D system of area  $L^2$ ,

$$\sum_{\mathbf{k}} A_{\mathbf{k}} \rightarrow \frac{L^2}{(2\pi)^2} \int_{\text{FS}} dk_{\parallel} \int dk_{\perp} A(k_{\parallel}, k_{\perp}) \quad (\text{B1})$$

$$\approx \frac{L^2}{\hbar(2\pi)^2} \int_{\text{FS}} dk_{\parallel} \int_{-\infty}^{\infty} d\xi \frac{1}{|\mathbf{v}_{F,k_{\parallel}}|} A(k_{\parallel}, \xi), \quad (\text{B2})$$

with the  $\xi$  integral carried out in closed form, and the remaining  $k_{\parallel}$  integral expressed as a Fermi surface average. Implicit in this conversion is that the Fermi velocity  $\mathbf{v}_{F,k_{\parallel}}$  not go to zero anywhere on the Fermi surface, and that the kernel of the integral,  $A(k_{\parallel}, \xi)$ , die off fast enough that the  $\xi$  integral not extend beyond the boundary of the irreducible Brillouin zone.

These requirements fail spectacularly in LSCO, which undergoes a Lifshitz transition at  $p \approx 19\%$  when the van Hove singularity (vHS) passes through the Fermi energy, as shown in Fig. 11(d). For our realistic disorder model, in which the calculated scattering rates and self-energies [e.g., in Eqs. (6) and (7)] are highly sensitive to the density of final states, the consequences of persisting with Fermi surface averages can be dire. This is seen in Figs. 11(a)–11(c) for LSCO. When the calculation is restricted to the Fermi surface, the normal-state scattering rate  $(\Gamma_N)_{\text{FS}}$  diverges at the vHS; the required pairing strength, parameterized by the clean-limit transition temper-

TABLE I. Impurity parameters for the apical oxygen vacancy,  $V_O$ , in LSCO. *Ab initio* potentials from Wannier-projected DFT are tabulated in units of the DFT-derived nearest-neighbor hopping,  $|t| = 524.7$  meV, at three hole doping levels: the undoped  $\text{La}_{36}\text{Cu}_{18}\text{O}_{71}$  supercell;  $p_{\text{vH}}$ , with the van Hove singularity tuned to the Fermi level; and  $p_{\text{vH}} + 7\%$ . Representative values of the coordinates  $\mathbf{R}$  and  $\mathbf{R}'$  are given in a coordinate system where the defect is located a distance  $z$  above the origin. For  $V_O^{\text{near}}$  ( $z = 2.4$  Å), the origin is centered on a Cu site. For  $V_O^{\text{far}}$  ( $z = 4.2$  Å), the origin is centered on a  $\text{CuO}_2$  plaquette. Additional, symmetry-related copies are implied, and when included produce the momentum-dependent form factors shown, with momenta in units of  $1/a$ , the inverse lattice parameter. For the site-energy terms, the form factors depend only on the momentum transfer  $\mathbf{q} = \mathbf{k} - \mathbf{k}'$ . Form factors for the hopping modifications depend on  $\mathbf{k}$  and  $\mathbf{k}'$  separately.

Defect & location	Impurity term	Representative coordinates		Impurity potential $\Delta E/ t  \times 1000$			Form factor	Form factor
		$\mathbf{R}/a$	$\mathbf{R}'/a$	Undoped	$p_{\text{vH}}$	$p_{\text{vH}} + 7\%$	$f(\mathbf{q})$ or $f(\mathbf{k}, \mathbf{k}')$	$f(\mathbf{q} = 0) \equiv f(\mathbf{k} = \mathbf{k}')$
$V_O^{\text{near}}$	$V_0 = V_{\mathbf{R}}$	(0,0)	–	–323.96	–358.68	–381.55	1	1
$z = 2.4$ Å	$V_2 = V_{\mathbf{R}}$	(1,0)	–	–104.36	–12.90	–25.40	$2[\cos(q_x) + \cos(q_y)]$	4
site-	$V_4 = V_{\mathbf{R}}$	(1,1)	–	–39.01	11.09	–13.77	$4 \cos(q_x) \cos(q_y)$	4
centered	$\delta t_0 = \delta t_{\mathbf{R}, \mathbf{R}'}$	(0,0)	(1,0)	8.08	14.83	16.52	$2[\cos(k_x) + \cos(k_y) + \cos(k'_x) + \cos(k'_y)]$	$4[\cos(k_x) + \cos(k_y)]$
	$\delta t_2 = \delta t_{\mathbf{R}, \mathbf{R}'}$	(1,0)	(1,1)	4.97	8.96	9.64	$4(\cos(k_x - k'_x)[\cos(k_y) + \cos(k'_y)] + \cos(k_y - k'_y)[\cos(k_x) + \cos(k'_x)])$	$8[\cos(k_x) + \cos(k_y)]$
	$\delta t'_0 = \delta t_{\mathbf{R}, \mathbf{R}'}$	(0,0)	(1,1)	4.36	3.20	4.84	$4[\cos(k_x) \cos(k_y) + \cos(k'_x) \cos(k'_y)]$	$8 \cos(k_x) \cos(k_y)$
$V_O^{\text{far}}$	$V_1 = V_{\mathbf{R}}$	$(\frac{1}{2}, \frac{1}{2})$	–	–52.48	–45.78	–59.18	$4 \cos(\frac{q_x}{2}) \cos(\frac{q_y}{2})$	4
$z = 4.2$ Å	$V_3 = V_{\mathbf{R}}$	$(\frac{1}{2}, \frac{3}{2})$	–	–13.59	–7.72	–17.31	$4[\cos(\frac{q_x}{2}) \cos(\frac{3q_y}{2}) + \cos(\frac{3q_x}{2}) \cos(\frac{q_y}{2})]$	8
plaquette-								8
centered	$\delta t_1 = \delta t_{\mathbf{R}, \mathbf{R}'}$	$(\frac{1}{2}, \frac{1}{2})$	$(\frac{1}{2}, -\frac{1}{2})$	12.29	18.68	20.09	$8[\cos(\frac{k_x+k_y}{2}) \cos(\frac{k'_x-k'_y}{2}) + \cos(\frac{k_x-k_y}{2}) \cos(\frac{k'_x+k'_y}{2})]$	$8[\cos(k_x) + \cos(k_y)]$
	$\delta t_3 = \delta t_{\mathbf{R}, \mathbf{R}'}$	$(\frac{1}{2}, \frac{1}{2})$	$(\frac{1}{2}, \frac{3}{2})$	5.95	5.85	6.21	$4[\cos(\frac{2k_x+2k_y-k'_x-k'_y}{2}) \cos(\frac{k_x-k_y}{2}) + \cos(\frac{2k_x-2k_y-k'_x+k'_y}{2}) \cos(\frac{k_x+k_y}{2}) + \cos(\frac{k_x+k_y-2k'_x-2k'_y}{2}) \cos(\frac{k'_x-k'_y}{2}) + \cos(\frac{k_x-k_y-2k'_x+2k'_y}{2}) \cos(\frac{k'_x+k'_y}{2})]$	$8[\cos(k_x) + \cos(k_y)]$
	$\delta t'_1 = \delta t_{\mathbf{R}, \mathbf{R}'}$	$(\frac{1}{2}, \frac{1}{2})$	$(-\frac{1}{2}, -\frac{1}{2})$	3.66	1.01	0.51	$8 \cos(\frac{k_x+k'_x}{2}) \cos(\frac{k_y+k'_y}{2})$	$8 \cos(k_x) \cos(k_y)$

ature  $T_{c0}(p)$ , has a sharp peak; and the zero-temperature superfluid density,  $\rho_s(T = 0)$ , is driven to zero. None of these effects is physical or in accord with experiment. By contrast,

when the momentum-sum method is used,  $(\Gamma_N)_{\text{FS}}$ ,  $T_{c0}$  and  $\rho_s(T = 0)$  pass smoothly and monotonically through the vHS. Well away from the vHS, the Fermi-surface calculations agree

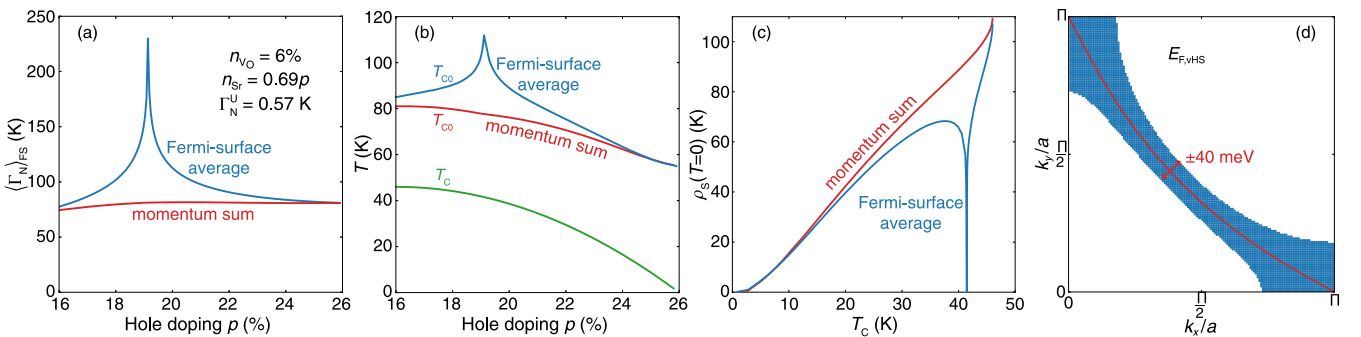


FIG. 11. Comparison of Fermi-surface-average and momentum-sum methods in LSCO, in the vicinity of the van Hove singularity (vHS) at hole doping  $p = 19\%$ . (a) Average normal-state scattering rate,  $(\Gamma_N)_{\text{FS}}$ . (b) Clean-limit transition temperatures  $T_{c0}(p)$  required to produce the parabolic dome of transition temperature,  $T_c(p)$ . (c) Resulting zero-temperature superfluid density,  $\rho_s(T = 0)$ . (d) One quadrant of the 2D Brillouin zone, at the Lifshitz transition ( $p = 19\%$ ), schematically showing how the momentum sum (discrete points) can be implemented using an energy cutoff of  $\pm 40$  meV about the Fermi surface (solid line). The plots in panels (a–c) use the disorder parameters shown in panel (a).

TABLE II. Impurity parameters for the Sr dopant in LSCO. *Ab-initio* potentials from Wannier-projected DFT are tabulated in units of the DFT-derived nearest-neighbor hopping,  $|t| = 524.7$  meV, at three hole-doping levels: the undoped  $\text{La}_{35}\text{SrCu}_{18}\text{O}_{72}$  supercell;  $p_{\text{vH}}$ , with the van Hove singularity tuned to the Fermi level; and  $p_{\text{vH}} + 7\%$ . Representative values of the coordinates  $\mathbf{R}$  and  $\mathbf{R}'$  are given in a coordinate system where the defect is located a distance  $z$  above the origin. For  $\text{Sr}^{\text{near}}$  ( $z = 1.8$  Å), the origin is centered on a  $\text{CuO}_2$  plaquette. For  $\text{Sr}^{\text{far}}$  ( $z = 4.8$  Å), the origin is centered on a Cu atom. Additional, symmetry-related copies are implied, and when included produce the momentum-dependent form factors shown, with momenta in units of  $1/a$ , the inverse lattice parameter.

Defect & location	Impurity term	Representative coordinates		Impurity potential $\Delta E/ t  \times 1000$			Form factor $f(\mathbf{q})$ or $f(\mathbf{k}, \mathbf{k}')$	Form factor $f(\mathbf{q} = 0) \equiv f(\mathbf{k} = \mathbf{k}')$
		$\mathbf{R}/a$	$\mathbf{R}'/a$	Undoped	$p_{\text{vH}}$	$p_{\text{vH}} + 7\%$		
$\text{Sr}^{\text{near}}$ $z = 1.8$ Å plaquette-centered	$V_1 = V_{\mathbf{R}}$	$(\frac{1}{2}, \frac{1}{2})$	–	97.56	70.80	69.44	$4 \cos(\frac{q_x}{2}) \cos(\frac{q_y}{2})$	4
	$V_3 = V_{\mathbf{R}}$	$(\frac{1}{2}, \frac{3}{2})$	–	18.28	6.99	7.73	$4 \left[ \cos(\frac{q_x}{2}) \cos(\frac{3q_y}{2}) + \cos(\frac{3q_x}{2}) \cos(\frac{q_y}{2}) \right]$	8
	$\delta t_1 = \delta t_{\mathbf{R}, \mathbf{R}'}$	$(\frac{1}{2}, \frac{1}{2})$	$(\frac{1}{2}, -\frac{1}{2})$	–27.84	–29.81	–30.18	$8 \left[ \cos(\frac{k_x+k_y}{2}) \cos(\frac{k'_x-k'_y}{2}) + \cos(\frac{k_x-k_y}{2}) \cos(\frac{k'_x+k'_y}{2}) \right]$	$8[\cos(k_x) + \cos(k_y)]$
	$\delta t_3 = \delta t_{\mathbf{R}, \mathbf{R}'}$	$(\frac{1}{2}, \frac{1}{2})$	$(\frac{1}{2}, \frac{3}{2})$	–18.14	–15.79	–14.21	$4 \left[ \cos(\frac{2k_x+2k_y-k'_x-k'_y}{2}) \cos(\frac{k_x-k_y}{2}) + \cos(\frac{2k_x-2k_y-k'_x+k'_y}{2}) \cos(\frac{k_x+k_y}{2}) + \cos(\frac{k_x+k_y-2k'_x-2k'_y}{2}) \cos(\frac{k'_x-k'_y}{2}) + \cos(\frac{k_x-k_y-2k'_x+2k'_y}{2}) \cos(\frac{k'_x+k'_y}{2}) \right]$	$8[\cos(k_x) + \cos(k_y)]$
	$\delta t'_1 = \delta t_{\mathbf{R}, \mathbf{R}'}$	$(\frac{1}{2}, \frac{1}{2})$	$(-\frac{1}{2}, -\frac{1}{2})$	–5.77	–5.78	–5.40	$8 \cos(\frac{k_x+k'_x}{2}) \cos(\frac{k_y+k'_y}{2})$	$8 \cos(k_x) \cos(k_y)$
$\text{Sr}^{\text{far}}$ $z = 4.8$ Å site-centered	$V_0 = V_{\mathbf{R}}$	(0,0)	–	30.83	–9.12	–22.24	1	1
	$V_2 = V_{\mathbf{R}}$	(1,0)	–	15.71	–4.57	–3.86	$2[\cos(q_x) + \cos(q_y)]$	4
	$V_4 = V_{\mathbf{R}}$	(1,1)	–	15.79	0.62	3.33	$4 \cos(q_x) \cos(q_y)$	4
	$\delta t_0 = \delta t_{\mathbf{R}, \mathbf{R}'}$	(0,0)	(1,0)	–10.03	–9.81	–8.96	$2[\cos(k_x) + \cos(k_y) + \cos(k'_x) + \cos(k'_y)]$	$4[\cos(k_x) + \cos(k_y)]$
	$\delta t_2 = \delta t_{\mathbf{R}, \mathbf{R}'}$	(1,0)	(1,1)	–7.16	–6.28	–5.47	$4(\cos(k_x - k'_x)[\cos(k_y) + \cos(k'_y)] + \cos(k_y - k'_y)[\cos(k_x) + \cos(k'_x)])$	$8[\cos(k_x) + \cos(k_y)]$
	$\delta t'_0 = \delta t_{\mathbf{R}, \mathbf{R}'}$	(0,0)	(1,1)	–1.75	–1.31	–0.47	$4[\cos(k_x) \cos(k_y) + \cos(k'_x) \cos(k'_y)]$	$8 \cos(k_x) \cos(k_y)$

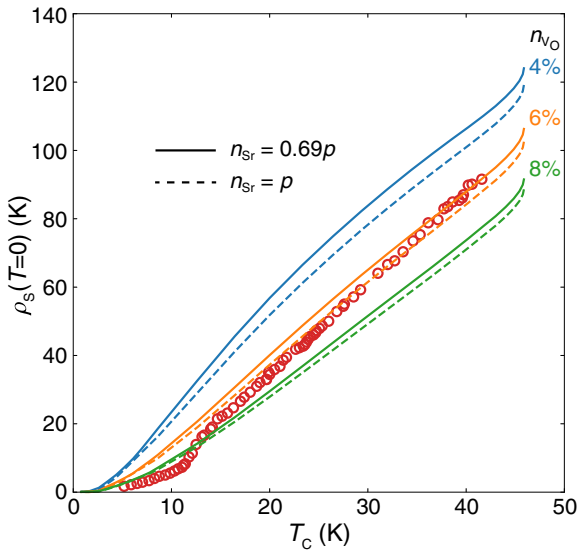


FIG. 12. The effect of Sr and apical-oxygen-vacancy concentration on the superfluid density of LSCO. Solid lines are calculated using the doping relation from ARPES Fermi volume,  $n_{\text{Sr}} = 0.69p$ ; dashed lines are based on the conventional doping dependence,  $n_{\text{Sr}} = p$ .  $n_{\text{vO}} = 4, 6,$  and  $8\%$  and  $\Gamma_N^u = 0.57$  K. Experimental data from Ref. [3].

with the momentum-sum method but, as Figs. 11(a)–11(c) show, the anomalies associated with the vHS persist over a surprisingly wide range, so caution is warranted.

Momentum sums are computationally more expensive than Fermi-surface averaging. To mitigate this, after taking advantage of symmetry to down-fold all sums into the irreducible octant, an energy cutoff can be implemented to eliminate unneeded  $k$ -points, on the basis that the kernels of the sums fall off sufficiently rapidly with  $\xi_{\mathbf{k}}$ . We have verified this by testing for convergence, with the result that an energy cutoff of 40 meV safely eliminates any cutoff dependence. In calculations of the sort presented here, the coarse-grained and energy-cut-off momentum sum typically consists of 4700  $k$ -points within the irreducible octant. Figure 11(d) illustrates the situation in LSCO, showing how the  $\mathbf{k}$ -sum method nicely regularizes the approach to the vHS at the  $(\pi, 0)$  point. However, for completeness, the energy cutoff was removed for the final calculations presented in the paper, which were carried out using full-Brillouin-zone sums consisting of approximately 12000 points.

### APPENDIX C: EFFECT OF $V_{\text{O}}$ AND SR CONCENTRATION IN LSCO

The effect of Sr dopant and apical-oxygen-vacancy concentration on the zero-temperature superfluid density of

TABLE III. Impurity parameters for Cu substituted onto the Tl site in Tl-2201. *Ab initio* potentials from Wannier-projected DFT are tabulated in units of the DFT-derived nearest-neighbor hopping,  $|t| = 537.8$  meV, for a  $\text{Tl}_{35}\text{Ba}_{36}\text{Cu}_{19}\text{O}_{108}$  supercell. Representative values of the coordinates  $\mathbf{R}$  and  $\mathbf{R}'$  are given in a coordinate system where the defect is located a distance  $z$  above the origin. For  $\text{Cu}^{\text{near}}$  ( $z = 4.7$  Å), the origin is centered on a Cu site. For  $\text{Cu}^{\text{far}}$  ( $z = 6.9$  Å), the origin is centered on a  $\text{CuO}_2$  plaquette. Additional, symmetry-related copies are implied, and when included produce the momentum-dependent form factors shown, with momenta in units of  $1/a$ , the inverse lattice parameter.

Defect & location	Impurity term	Rep. coords.		Impurity potential $\Delta E/ t  \times 1000$	Form factor $f(\mathbf{q})$ or $f(\mathbf{k}, \mathbf{k}')$	Form factor $f(\mathbf{q} = 0) \equiv f(\mathbf{k} = \mathbf{k}')$
		$\mathbf{R}/a$	$\mathbf{R}'/a$			
$\text{Cu}^{\text{near}}$ $z = 4.7$ Å site-centered	$V_0 = V_{\mathbf{R}}$	(0,0)	–	155.72	1	1
	$V_2 = V_{\mathbf{R}}$	(1,0)	–	77.50	$2[\cos(q_x) + \cos(q_y)]$	4
	$V_4 = V_{\mathbf{R}}$	(1,1)	–	66.97	$4 \cos(q_x) \cos(q_y)$	4
	$\delta t_0 = \delta t_{\mathbf{R}, \mathbf{R}'}$	(0,0)	(1,0)	–9.15	$2[\cos(k_x) + \cos(k_y) + \cos(k'_x) + \cos(k'_y)]$	$4[\cos(k_x) + \cos(k_y)]$
	$\delta t_2 = \delta t_{\mathbf{R}, \mathbf{R}'}$	(1,0)	(1,1)	–7.39	$4(\cos(k_x - k'_x)[\cos(k_y) + \cos(k'_y)] + \cos(k_y - k'_y)[\cos(k_x) + \cos(k'_x)])$	$8[\cos(k_x) + \cos(k_y)]$
	$\delta t'_0 = \delta t_{\mathbf{R}, \mathbf{R}'}$	(0,0)	(1,1)	–2.88	$4[\cos(k_x) \cos(k_y) + \cos(k'_x) \cos(k'_y)]$	$8 \cos(k_x) \cos(k_y)$
$\text{Cu}^{\text{far}}$ $z = 6.9$ Å plaquette-centered	$V_1 = V_{\mathbf{R}}$	$(\frac{1}{2}, \frac{1}{2})$	–	100.50	$4 \cos(\frac{q_x}{2}) \cos(\frac{q_y}{2})$	4
	$V_3 = V_{\mathbf{R}}$	$(\frac{1}{2}, \frac{3}{2})$	–	37.29	$4[\cos(\frac{q_x}{2}) \cos(\frac{3q_y}{2}) + \cos(\frac{3q_x}{2}) \cos(\frac{q_y}{2})]$	8
	$\delta t_1 = \delta t_{\mathbf{R}, \mathbf{R}'}$	$(\frac{1}{2}, \frac{1}{2})$	$(\frac{1}{2}, -\frac{1}{2})$	–6.45	$8[\cos(\frac{k_x+k_y}{2}) \cos(\frac{k'_x-k'_y}{2}) + \cos(\frac{k_x-k_y}{2}) \cos(\frac{k'_x+k'_y}{2})]$	$8[\cos(k_x) + \cos(k_y)]$
	$\delta t_3 = \delta t_{\mathbf{R}, \mathbf{R}'}$	$(\frac{1}{2}, \frac{1}{2})$	$(\frac{1}{2}, \frac{3}{2})$	–2.83	$4[\cos(\frac{2k_x+2k_y-k'_x-k'_y}{2}) \cos(\frac{k_x-k_y}{2}) + \cos(\frac{2k_x-2k_y-k'_x+k'_y}{2}) \cos(\frac{k_x+k_y}{2}) + \cos(\frac{k_x+k_y-2k'_x-2k'_y}{2}) \cos(\frac{k'_x-k'_y}{2}) + \cos(\frac{k_x-k_y-2k'_x+2k'_y}{2}) \cos(\frac{k'_x+k'_y}{2})]$	$8[\cos(k_x) + \cos(k_y)]$
	$\delta t'_1 = \delta t_{\mathbf{R}, \mathbf{R}'}$	$(\frac{1}{2}, \frac{1}{2})$	$(-\frac{1}{2}, -\frac{1}{2})$	–0.89	$8 \cos(\frac{k_x+k'_x}{2}) \cos(\frac{k_y+k'_y}{2})$	$8 \cos(k_x) \cos(k_y)$

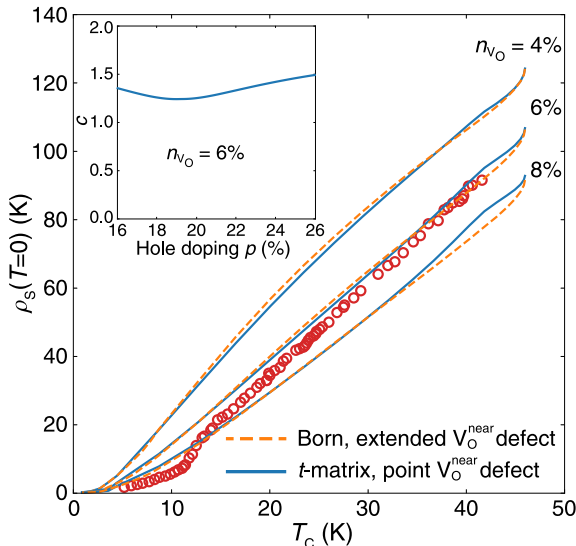


FIG. 13. Zero-temperature superfluid density for LSCO, calculated by treating the near apical oxygen vacancy,  $V_{\text{O}}^{\text{near}}$ , alternately in the  $t$ -matrix and Born approximations. In the  $t$ -matrix approximation (solid lines),  $V_{\text{O}}^{\text{near}}$  is modelled by an intermediate-strength point scatterer of scattering parameter  $c$ . In the Born approximation (dashed lines), the full extended impurity potential  $n_{V_{\text{O}}} = 4, 6,$  and  $8\%$ ,  $n_{\text{Sr}} = 0.69p$  and  $\Gamma_N^u = 0.57$  K. Experimental data from Ref. [3]. Inset:  $c = \cot \delta$  for the  $V_{\text{O}}^{\text{near}}$  impurity, for  $n_{V_{\text{O}}} = 6\%$ .

LSCO is shown in Fig. 12. Two doping dependencies of the Sr concentration are compared: one derived from ARPES Fermi volume,  $n_{\text{Sr}} = 0.69p$ ; and the conventional relation,  $n_{\text{Sr}} = p$ . The impurity potential of the Sr dopants, which is extended in real space and therefore inherently forward scattering, does not have a strong pair-breaking effect, with the superfluid density relatively insensitive to changes in Sr concentration. Results are also shown for three different concentrations of apical oxygen vacancy. This defect, which has a nearly point-like impurity potential, causes significant pair breaking.

#### APPENDIX D: EFFECT OF INTERMEDIATE-STRENGTH SCATTERERS

As mentioned in Sec. IV, a possible shortcoming of the approach taken in the current paper is that we have treated the out-of-plane dopant impurities in the Born approximation, where the perturbation series for their self energies, Eqs. (6) and (7), are truncated at second order. This makes the calculation of vertex corrections tractable, and becomes exact in the weak-scattering limit,  $V_{\text{imp}}N_0 \ll 1$ . A better approach would be to study these impurities in the  $t$ -matrix approximation where, by summing the perturbation series to all orders, arbitrary scattering strengths could be accurately accounted for. This is unfortunately beyond the scope of the current paper, due to the computational cost of implementing vertex corrections in the full  $t$ -matrix approximation.

To test the adequacy of the Born approximation, we focus on the strongest out-of-plane scatterer in LSCO, the near

apical oxygen vacancy,  $V_{\text{O}}^{\text{near}}$ . As can be seen in Table I, the impurity potential for  $V_{\text{O}}^{\text{near}}$  is nearly pointlike, with  $V_{\text{imp}} = V_0 \gg V_2, V_4, \dots$ . To good approximation this enables us to treat the  $V_{\text{O}}^{\text{near}}$  defects as point scatterers, and therefore to use the  $t$ -matrix approximation. The contribution of  $V_{\text{O}}^{\text{near}}$  to the  $\tau_0$  self energy in the point-scattering limit then takes the form

$$\Sigma_0^{t\text{-matrix}} = \Gamma \frac{G_0}{c^2 + G_0^2}, \quad (\text{D1})$$

where  $\Gamma = n_{V_{\text{O}}}/(\pi N_0)$  parameterizes the concentration of the apical oxygen vacancies, and  $c = 1/(\pi V_{\text{imp}} N_0)$  is the cotangent of the scattering phase shift.

To implement the  $t$ -matrix approximation for the near apical oxygen vacancies, the Born term for  $V_{\text{O}}^{\text{near}}$  in Eq. (6) is

replaced by Eq. (D1). Note that for point scatterers there is no contribution to explicit gap renormalization in Eq. (7), and no contribution to vertex corrections. Figure 13 shows the results for zero-temperature superfluid density in LSCO. Born and  $t$ -matrix approximations are in very close agreement over the whole doping range, with a small deviation in the vicinity of the van Hove doping. The doping dependence of the  $V_{\text{O}}^{\text{near}}$  scattering parameter, plotted in the inset of Fig. 13, shows the reason for the deviation:  $c(p)$  has a small dip near  $p = 19\%$  as a result of the van-Hove enhancement of  $N_0$  at this doping.

Referring to Table II, we see that the impurity potential for  $\text{Sr}^{\text{near}}$  is significantly weaker than for  $V_{\text{O}}^{\text{near}}$ , even taking into account that the plaquette-centered  $\text{Sr}^{\text{near}}$  affects its nearest four Cu neighbors equally. We are therefore confident that although the out-of-plane defects approach intermediate scattering strength ( $c \sim 1$ ), the Born approximation remains valid.

### APPENDIX E: DISORDER RENORMALIZATION OF TWO-PARTICLE PROPERTIES

Within the ladder approximation, the current vertex  $\Lambda(\mathbf{k}, \omega_n)$  can be approximated by a sum of ladder diagrams and then resolved into components  $\gamma_0, \gamma_1$  and  $\gamma_3$  in particle-hole space [38,39]:

$$\Lambda(\mathbf{k}, \omega_n) = \mathbf{v}_{\mathbf{k}} \tau_0 + \frac{1}{N} \sum_{\mathbf{k}'} \sum_i n_i |V_{\mathbf{k}, \mathbf{k}'}^i|^2 \mathbf{v}_{\mathbf{k}'}^j \tau_3 \underline{G}(\mathbf{k}', \omega_n) \Lambda(\mathbf{k}', \omega_n) \underline{G}(\mathbf{k}', \omega_n) \tau_3, \quad (\text{E1})$$

$$\gamma_0(\mathbf{k}, \omega_n) = 1 + \frac{1}{N} \sum_{\mathbf{k}'} \sum_i s_{\mathbf{k}, \mathbf{k}'} n_i |V_{\mathbf{k}, \mathbf{k}'}^i|^2 \frac{\gamma_0(\mathbf{k}', \omega_n) (\tilde{\Delta}_{\mathbf{k}'n}^2 + \xi_{\mathbf{k}'}^2 - \tilde{\omega}_{\mathbf{k}'n}^2) - 2\gamma_1(\mathbf{k}', \omega_n) \tilde{\Delta}_{\mathbf{k}'n} \tilde{\omega}_{\mathbf{k}'n} + 2i\gamma_3(\mathbf{k}', \omega_n) \xi_{\mathbf{k}'} \tilde{\omega}_{\mathbf{k}'n}}{(\tilde{\Delta}_{\mathbf{k}'n}^2 + \xi_{\mathbf{k}'}^2 + \tilde{\omega}_{\mathbf{k}'n}^2)^2}, \quad (\text{E2})$$

$$\gamma_1(\mathbf{k}, \omega_n) = \frac{1}{N} \sum_{\mathbf{k}'} \sum_i s_{\mathbf{k}, \mathbf{k}'} n_i |V_{\mathbf{k}, \mathbf{k}'}^i|^2 \frac{-2\gamma_0(\mathbf{k}', \omega_n) \tilde{\Delta}_{\mathbf{k}'n} \tilde{\omega}_{\mathbf{k}'n} + \gamma_1(\mathbf{k}', \omega_n) (-\tilde{\Delta}_{\mathbf{k}'n}^2 + \xi_{\mathbf{k}'}^2 + \tilde{\omega}_{\mathbf{k}'n}^2) + 2i\gamma_3(\mathbf{k}', \omega_n) \xi_{\mathbf{k}'} \tilde{\Delta}_{\mathbf{k}'n}}{(\tilde{\Delta}_{\mathbf{k}'n}^2 + \xi_{\mathbf{k}'}^2 + \tilde{\omega}_{\mathbf{k}'n}^2)^2}, \quad (\text{E3})$$

$$\gamma_3(\mathbf{k}, \omega_n) = \frac{1}{N} \sum_{\mathbf{k}'} \sum_i s_{\mathbf{k}, \mathbf{k}'} n_i |V_{\mathbf{k}, \mathbf{k}'}^i|^2 \frac{2i\gamma_0(\mathbf{k}', \omega_n) \xi_{\mathbf{k}'} \tilde{\omega}_{\mathbf{k}'n} + 2i\gamma_1(\mathbf{k}', \omega_n) \tilde{\Delta}_{\mathbf{k}'n} \xi_{\mathbf{k}'} - \gamma_3(\mathbf{k}', \omega_n) (\tilde{\Delta}_{\mathbf{k}'n}^2 - \xi_{\mathbf{k}'}^2 + \tilde{\omega}_{\mathbf{k}'n}^2)}{(\tilde{\Delta}_{\mathbf{k}'n}^2 + \xi_{\mathbf{k}'}^2 + \tilde{\omega}_{\mathbf{k}'n}^2)^2}, \quad (\text{E4})$$

where  $s_{\mathbf{k}, \mathbf{k}'} = \mathbf{v}_{\mathbf{k}'}^j \cdot \mathbf{v}_{\mathbf{k}}^j / |\mathbf{v}_{\mathbf{k}}^j|^2$ . When it is safe to assume a linearized spectrum  $\xi_{\mathbf{k}}$ , the  $\xi$  integrations in Eqs. (E1) to (E4) can be carried out, allowing the vertex functions to be recast as Fermi surface averages:

$$\Lambda(\mathbf{k}, \omega_n) = \mathbf{v}_{\mathbf{k}} \tau_0 + N_0 \left\langle \sum_i n_i |V_{\mathbf{k}, \mathbf{k}'}^i|^2 \mathbf{v}_{\mathbf{k}'}^j \tau_3 \underline{G}(\mathbf{k}', \omega_n) \Lambda(\mathbf{k}', \omega_n) \underline{G}(\mathbf{k}', \omega_n) \tau_3 \right\rangle_{\text{FS}_{\mathbf{k}'}} , \quad (\text{E5})$$

$$\gamma_0(\mathbf{k}, \omega_n) = 1 + N_0 \left\langle \sum_i n_i |V_{\mathbf{k}, \mathbf{k}'}^i|^2 s_{\mathbf{k}, \mathbf{k}'} \frac{\tilde{\Delta}_{\mathbf{k}'n}^2 \gamma_0(\mathbf{k}', \omega_n) - \tilde{\Delta}_{\mathbf{k}'n} \tilde{\omega}_{\mathbf{k}'n} \gamma_1(\mathbf{k}', \omega_n)}{(\tilde{\omega}_{\mathbf{k}'n}^2 + \tilde{\Delta}_{\mathbf{k}'n}^2)^{3/2}} \right\rangle_{\text{FS}_{\mathbf{k}'}} , \quad (\text{E6})$$

$$\gamma_1(\mathbf{k}, \omega_n) = -N_0 \left\langle \sum_i n_i |V_{\mathbf{k}, \mathbf{k}'}^i|^2 s_{\mathbf{k}, \mathbf{k}'} \frac{\tilde{\Delta}_{\mathbf{k}'n} \tilde{\omega}_{\mathbf{k}'n} \gamma_0(\mathbf{k}', \omega_n) - \tilde{\omega}_{\mathbf{k}'n}^2 \gamma_1(\mathbf{k}', \omega_n)}{(\tilde{\omega}_{\mathbf{k}'n}^2 + \tilde{\Delta}_{\mathbf{k}'n}^2)^{3/2}} \right\rangle_{\text{FS}_{\mathbf{k}'}} , \quad (\text{E7})$$

$$\gamma_3(\mathbf{k}, \omega_n) = 0. \quad (\text{E8})$$

- [1] B. Keimer, S. A. Kivelson, M. R. Norman, S. Uchida, and J. Zaanen, From quantum matter to high-temperature superconductivity in copper oxides, *Nature* **518**, 179 (2015).
- [2] C. Proust and L. Taillefer, The remarkable underlying ground states of cuprate superconductors, *Annu. Rev. Condens. Matter Phys.* **10**, 409 (2019).
- [3] I. Božović, X. He, J. Wu, and A. T. Bollinger, Dependence of the critical temperature in overdoped copper oxides on superfluid density, *Nature* **536**, 309 (2016).

- [4] F. Mahmood, X. He, I. Božović, and N. P. Armitage, Locating the Missing Superconducting Electrons in Overdoped Cuprates, *Phys. Rev. Lett.* **122**, 027003 (2019).
- [5] N. R. Lee-Hone, J. S. Dodge, and D. M. Broun, Disorder and superfluid density in overdoped cuprate superconductors, *Phys. Rev. B* **96**, 024501 (2017).
- [6] N. R. Lee-Hone, V. Mishra, D. M. Broun, and P. J. Hirschfeld, Optical conductivity of overdoped cuprate superconductors: Application to  $\text{La}_{2-x}\text{Sr}_x\text{CuO}_4$ , *Phys. Rev. B* **98**, 054506 (2018).



- [7] N. R. Lee-Hone, H. U. Özdemir, V. Mishra, D. M. Broun, and P. J. Hirschfeld, Low-energy phenomenology of the overdoped cuprates: Viability of the Landau-BCS paradigm, *Phys. Rev. Res.* **2**, 013228 (2020).
- [8] P. J. Hirschfeld and N. Goldenfeld, Effect of strong scattering on the low-temperature penetration depth of a  $d$ -wave superconductor, *Phys. Rev. B* **48**, 4219 (1993).
- [9] P. Arberg, M. Mansor, and J. P. Carbotte, Penetration depth for a 2D  $d$ -wave superconductor, *Solid State Commun.* **86**, 671 (1993).
- [10] I. Božović, A. T. Bollinger, J. Wu, and X. He, Can high- $T_c$  superconductivity in cuprates be explained by the conventional BCS theory? *Low Temp. Phys.* **44**, 519 (2018).
- [11] D. C. Peets, R.-X. Liang, M. Raudsepp, W. N. Hardy, and D. A. Bonn, Encapsulated single crystal growth and annealing of the high-temperature superconductor Tl-2201, *J. Cryst. Growth* **312**, 344 (2010).
- [12] K. Fujita, T. Noda, K. M. Kojima, H. Eisaki, and S. Uchida, Effect of Disorder Outside the CuO<sub>2</sub> Planes on  $T_c$  of Copper Oxide Superconductors, *Phys. Rev. Lett.* **95**, 097006 (2005).
- [13] F. Rullier-Albenque, H. Alloul, F. Balakirev, and C. Proust, Disorder, metal-insulator crossover and phase diagram in high- $T_c$  cuprates, *Europhys. Lett.* **81**, 37008 (2008).
- [14] D. Wang, J.-Q. Xu, H.-J. Zhang, and Q.-H. Wang, Anisotropic Scattering Caused by Apical Oxygen Vacancies in Thin Films of Overdoped High-Temperature Cuprate Superconductors, *Phys. Rev. Lett.* **128**, 137001 (2022).
- [15] H. U. Özdemir, V. Mishra, N. R. Lee-Hone, X. Kong, T. Berlijn, D. M. Broun, and P. J. Hirschfeld, Comment on “Anisotropic scattering caused by apical oxygen vacancies in thin films of overdoped high-temperature cuprate superconductors”, [arXiv:2206.01301](https://arxiv.org/abs/2206.01301).
- [16] T. Berlijn, D. Volja, and W. Ku, Can Disorder Alone Destroy the  $e'_g$  Hole Pockets of Na<sub>x</sub>CoO<sub>2</sub>? A Wannier Function Based First-Principles Method for Disordered Systems, *Phys. Rev. Lett.* **106**, 077005 (2011).
- [17] I. Mazin, Inverse Occam’s razor, *Nat. Phys.* **18**, 367 (2022).
- [18] P. R. C. Kent and G. Kotliar, Toward a predictive theory of correlated materials, *Science* **361**, 348 (2018).
- [19] J. W. Furness, Y. Zhang, C. Lane, I. G. Buda, B. Barbiellini, R. S. Markiewicz, A. Bansil, and J. Sun, An accurate first-principles treatment of doping-dependent electronic structure of high-temperature cuprate superconductors, *Commun. Phys.* **1**, 11 (2018).
- [20] T. Yoshida, X. J. Zhou, K. Tanaka, W. L. Yang, Z. Hussain, Z. X. Shen, A. Fujimori, S. Sahrakorpi, M. Lindroos, R. S. Markiewicz, A. Bansil, S. Komiya, Y. Ando, H. Eisaki, T. Kakeshita, and S. Uchida, Systematic doping evolution of the underlying Fermi surface of La<sub>2-x</sub>Sr<sub>x</sub>CuO<sub>4</sub>, *Phys. Rev. B* **74**, 224510 (2006).
- [21] T. Yoshida, X. J. Zhou, D. H. Lu, S. Komiya, Y. Ando, H. Eisaki, T. Kakeshita, S. Uchida, Z. Hussain, Z. X. Shen, and A. Fujimori, Low-energy electronic structure of the high- $T_c$  cuprates La<sub>2-x</sub>Sr<sub>x</sub>CuO<sub>4</sub> studied by angle-resolved photoemission spectroscopy, *J. Phys.: Condens. Matter* **19**, 125209 (2007).
- [22] M. Platé, J. D. F. Mottershead, I. S. Elfimov, D. C. Peets, R. Liang, D. A. Bonn, W. N. Hardy, S. Chiuzbaian, M. Falub, M. Shi, L. Patthey, and A. Damascelli, Fermi Surface and Quasiparticle Excitations of Overdoped Tl<sub>2</sub>Ba<sub>2</sub>CuO<sub>6+δ</sub>, *Phys. Rev. Lett.* **95**, 077001 (2005).
- [23] N. Momono, M. Ido, T. Nakano, M. Oda, Y. Okajima, and K. Yamaya, Low-temperature electronic specific heat of La<sub>2-x</sub>Sr<sub>x</sub>CuO<sub>4</sub> and La<sub>2-x</sub>Sr<sub>x</sub>Cu<sub>1-y</sub>Zn<sub>y</sub>O<sub>4</sub>. Evidence for a  $d$ -wave superconductor, *Physica C* **233**, 395 (1994).
- [24] Y. Wang, J. Yan, L. Shan, H.-H. Wen, Y. Tanabe, T. Adachi, and Y. Koike, Weak-coupling  $d$ -wave BCS superconductivity and unpaired electrons in overdoped La<sub>2-x</sub>Sr<sub>x</sub>CuO<sub>4</sub> single crystals, *Phys. Rev. B* **76**, 064512 (2007).
- [25] T. Berlijn, C.-H. Lin, W. Garber, and W. Ku, Do Transition-Metal Substitutions Dope Carriers in Iron-Based Superconductors? *Phys. Rev. Lett.* **108**, 207003 (2012).
- [26] L. Wang, T. Berlijn, Y. Wang, C.-H. Lin, P. J. Hirschfeld, and W. Ku, Effects of Disordered Ru Substitution in BaFe<sub>2</sub>As<sub>2</sub>: Possible Realization of Superdiffusion in Real Materials, *Phys. Rev. Lett.* **110**, 037001 (2013).
- [27] T. Berlijn, H.-P. Cheng, P. J. Hirschfeld, and W. Ku, Doping effects of Se vacancies in monolayer FeSe, *Phys. Rev. B* **89**, 020501(R) (2014).
- [28] J. Chang, M. Mansson, S. Pailhès, T. Claesson, O. J. Lipscombe, S. M. Hayden, L. Patthey, O. Tjernberg, and J. Mesot, Anisotropic breakdown of Fermi liquid quasiparticle excitations in overdoped La<sub>2-x</sub>Sr<sub>x</sub>CuO<sub>4</sub>, *Nat. Commun.* **4**, 2559 (2013).
- [29] M. Horio, K. Hauser, Y. Sassa, Z. Mingazheva, D. Sutter, K. Kramer, A. Cook, E. Nocerino, O. K. Forslund, O. Tjernberg, M. Kobayashi, A. Chikina, N. B. M. Schröter, J. A. Krieger, T. Schmitt, V. N. Strocov, S. Pyon, T. Takayama, H. Takagi, O. J. Lipscombe *et al.*, Three-Dimensional Fermi Surface of Overdoped La-Based Cuprates, *Phys. Rev. Lett.* **121**, 077004 (2018).
- [30] J. B. Torrance, Y. Tokura, A. I. Nazzari, A. Bezinge, T. C. Huang, and S. S. P. Parkin, Anomalous Disappearance of High- $T_c$  Superconductivity at High Hole Concentration in Metallic La<sub>2-x</sub>Sr<sub>x</sub>CuO<sub>4</sub>, *Phys. Rev. Lett.* **61**, 1127 (1988).
- [31] I. Higashi and H. Kitazawa, Single-crystal x-ray diffraction analysis of (La<sub>1-x</sub>Sr<sub>x</sub>)<sub>2</sub>CuO<sub>4-δ</sub> ( $x = 0.047$ ), *Physica C* **185-189**, 551 (1991).
- [32] G. Kim, G. Christiani, G. Logvenov, S. Choi, H.-H. Kim, M. Minola, and B. Keimer, Selective formation of apical oxygen vacancies in La<sub>2-x</sub>Sr<sub>x</sub>CuO<sub>4</sub>, *Phys. Rev. Mater.* **1**, 054801 (2017).
- [33] R. S. Liu, S. D. Hughes, R. J. Angel, T. P. Hackwell, A. P. Mackenzie, and P. P. Edwards, Crystal structure and cation stoichiometry of superconducting Tl<sub>2</sub>Ba<sub>2</sub>CuO<sub>6+δ</sub> single crystals, *Physica C* **198**, 203 (1992).
- [34] N. N. Kolesnikov, V. E. Korotkov, M. P. Kulakov, R. P. Shibaeva, V. N. Molchanov, R. A. Tamazyan, and V. I. Simonov, Structure of superconducting single crystals of 2201 thallium cuprate (Tl<sub>1.85</sub>Cu<sub>0.15</sub>)Ba<sub>2</sub>CuO<sub>6</sub>,  $T_c = 110$  K, *Physica C* **195**, 219 (1992).
- [35] M. Hasegawa, H. Takei, K. Izawa, and Y. Matsuda, Crystal growth techniques for Tl-based cuprate superconductors, *J. Cryst. Growth* **229**, 401 (2001).
- [36] P. J. Hirschfeld, W. O. Putikka, and D. J. Scalapino,  $d$ -wave model for microwave response of high- $T_c$  superconductors, *Phys. Rev. B* **50**, 10250 (1994).

- [37] T. S. Nunner and P. J. Hirschfeld, Microwave conductivity of  $d$ -wave superconductors with extended impurities, *Phys. Rev. B* **72**, 014514 (2005).
- [38] S. Skalski, O. Betbeder-Matibet, and P. R. Weiss, Properties of superconducting alloys containing paramagnetic impurities, *Phys. Rev.* **136**, A1500 (1964).
- [39] A. C. Durst and P. A. Lee, Impurity-induced quasiparticle transport and universal-limit Wiedemann-Franz violation in  $d$ -wave superconductors, *Phys. Rev. B* **62**, 1270 (2000).
- [40] N. E. Hussey, J. R. Cooper, J. M. Wheatley, I. R. Fisher, A. Carrington, A. P. Mackenzie, C. T. Lin, and O. Milat, Angular Dependence of the  $c$ -axis Normal State Magnetoresistance in Single Crystal  $\text{Tl}_2\text{Ba}_2\text{CuO}_{6+\delta}$ , *Phys. Rev. Lett.* **76**, 122 (1996).
- [41] L. B. Ioffe and A. J. Millis, Zone-diagonal-dominated transport in high- $T_c$  cuprates, *Phys. Rev. B* **58**, 11631 (1998).
- [42] T. Valla, A. V. Fedorov, P. D. Johnson, Q. Li, G. D. Gu, and N. Koshizuka, Temperature-Dependent Scattering Rates at the Fermi Surface of Optimally Doped  $\text{Bi}_2\text{Sr}_2\text{CaCu}_2\text{O}_{8+\delta}$ , *Phys. Rev. Lett.* **85**, 828 (2000).
- [43] E. Abrahams and C. M. Varma, What angle-resolved photoemission experiments tell about the microscopic theory for high-temperature superconductors, *Proc. Natl. Acad. Sci.* **97**, 5714 (2000).
- [44] C. M. Varma and E. Abrahams, Effective Lorentz Force Due to Small-Angle Impurity Scattering: Magnetotransport in High- $T_c$  Superconductors, *Phys. Rev. Lett.* **86**, 4652 (2001).
- [45] A. Kaminski, H. M. Fretwell, M. R. Norman, M. Randeria, S. Rosenkranz, U. Chatterjee, J. C. Campuzano, J. Mesot, T. Sato, T. Takahashi, T. Terashima, M. Takano, K. Kadowaki, Z. Z. Li, and H. Raffy, Momentum anisotropy of the scattering rate in cuprate superconductors, *Phys. Rev. B* **71**, 014517 (2005).
- [46] M. Abdel-Jawad, M. P. Kennett, L. Balicas, A. Carrington, A. P. Mackenzie, R. H. Mckenzie, and N. E. Hussey, Anisotropic scattering and anomalous normal-state transport in a high-temperature superconductor, *Nat. Phys.* **2**, 821 (2006).
- [47] T. Yamasaki, K. Yamazaki, A. Ino, M. Arita, H. Namatame, M. Taniguchi, A. Fujimori, Z.-X. Shen, M. Ishikado, and S. Uchida, Unmasking the nodal quasiparticle dynamics in cuprate superconductors using low-energy photoemission, *Phys. Rev. B* **75**, 140513(R) (2007).
- [48] J. Chang, M. Shi, S. Pailh s, M. Mansson, T. Claesson, O. Tjernberg, A. Bendounan, Y. Sassa, L. Patthey, N. Momono, M. Oda, M. Ido, S. Guerrero, C. Mudry, and J. Mesot, Anisotropic quasiparticle scattering rates in slightly underdoped to optimally doped high-temperature  $\text{La}_{2-x}\text{Sr}_x\text{CuO}_4$  superconductors, *Phys. Rev. B* **78**, 205103 (2008).
- [49] G. Grissonnanche, Y. Fang, A. Legros, S. Verret, F. Lalibert , C. Collignon, J. Zhou, D. Graf, P. A. Goddard, L. Taillefer, and B. J. Ramshaw, Linear-in temperature resistivity from an isotropic Planckian scattering rate, *Nature* **595**, 667 (2021).
- [50] P. W. Anderson, Theory of dirty superconductors, *J. Phys. Chem. Solids* **11**, 26 (1959).
- [51] H. Y. Kee, Effect of doping-induced disorder on the transition temperature in high- $T_c$  cuprates, *Phys. Rev. B* **64**, 012506 (2001).
- [52] S. Graser, P. J. Hirschfeld, L. Y. Zhu, and T. Dahm,  $T_c$  suppression and resistivity in cuprates with out-of-plane defects, *Phys. Rev. B* **76**, 054516 (2007).
- [53] W. M. Li, J. F. Zhao, L. P. Cao, Z. Hu, Q. Z. Huang, X. C. Wang, Y. Liu, G. Q. Zhao, J. Zhang, Q. Q. Liu, R. Z. Yu, Y. W. Long, H. Wu, H. J. Lin, C. T. Chen, Z. Li, Z. Z. Gong, Z. Guguchia, J. S. Kim, G. R. Stewart *et al.*, Superconductivity in a unique type of copper oxide, *Proc. Natl. Acad. Sci. USA* **116**, 12156 (2019).
- [54] D. Deepwell, D. C. Peets, C. J. S. Truncik, N. C. Murphy, M. P. Kennett, W. A. Huttema, R. Liang, D. A. Bonn, W. N. Hardy, and D. M. Broun, Microwave conductivity and superfluid density in strongly overdoped  $\text{Tl}_2\text{Ba}_2\text{CuO}_{6+\delta}$ , *Phys. Rev. B* **88**, 214509 (2013).
- [55] J. H. Brewer, S. L. Stubbs, R. Liang, D. A. Bonn, W. N. Hardy, J. E. Sonier, W. A. MacFarlane, and D. C. Peets, Signatures of new  $d$ -wave vortex physics in overdoped  $\text{Tl}_2\text{Ba}_2\text{CuO}_{6+x}$  revealed by TF- $\mu^+$ SR, *Sci. Rep.* **5**, 14156 (2015).
- [56] C. Niedermayer, C. Bernhard, U. Binniger, H. Gl ckler, J. L. Tallon, E. J. Ansaldo, and J. I. Budnick, Muon Spin Rotation Study of the Correlation Between  $T_c$  and  $n_s/m^*$  in Overdoped  $\text{Tl}_2\text{Ba}_2\text{CuO}_{6+\delta}$ , *Phys. Rev. Lett.* **71**, 1764 (1993).
- [57] Y. J. Uemura, A. Keren, L. P. Le, G. M. Luke, W. D. Wu, Y. Kubo, T. Manako, Y. Shimakawa, M. Subramanian, J. L. Cobb, and J. T. Markert, Magnetic-field penetration depth in  $\text{Tl}_2\text{Ba}_2\text{CuO}_{6+\delta}$  in the overdoped regime, *Nature* **364**, 605 (1993).
- [58] Z.-X. Li, S. A. Kivelson, and D.-H. Lee, Superconductor-to-metal transition in overdoped cuprates, *npj Quantum Mater.* **6**, 36 (2021).
- [59] R. Photopoulos and R. Fr sard, A 3D tight-binding model for La-based cuprate superconductors, *Ann. Phys. (Berlin)* **531**, 1900177 (2019).
- [60] E. W. Huang, D. J. Scalapino, T. A. Maier, B. Moritz, and T. P. Devereaux, Decrease of  $d$ -wave pairing strength in spite of the persistence of magnetic excitations in the overdoped Hubbard model, *Phys. Rev. B* **96**, 020503(R) (2017).
- [61] T. A. Maier, S. Karakuzu, and D. J. Scalapino, Overdoped end of the cuprate phase diagram, *Phys. Rev. Res.* **2**, 033132 (2020).
- [62] Y. Li, A. Sapkota, P. M. Lozano, Z. Du, H. Li, Z. Wu, A. K. Kundu, B. L. Winn, S. Chi, M. Matsuda, M. Frontzek, I. Bo zovi , A. N. Pasupathy, I. K. Drozdov, K. Fujita, G. D. Gu, I. Zaliznyak, Q. Li, and J. M. Tranquada, Strongly-overdoped  $\text{La}_{2-x}\text{Sr}_x\text{CuO}_4$ : Evidence for Josephson-coupled grains of strongly-correlated superconductor, [arXiv:2205.01702](https://arxiv.org/abs/2205.01702).
- [63] B. Spivak, P. Oreto, and S. A. Kivelson, Theory of quantum metal to superconductor transitions in highly conducting systems, *Phys. Rev. B* **77**, 214523 (2008).
- [64] K. Fujita, A. Schmidt, E.-A. Kim, M. Lawler, D.-H. Lee, J. Davis, H. Eisaki, and S.-I. Uchida, Spectroscopic imaging STM studies of electronic structure in the superconducting and pseudogap phases of cuprate high- $T_c$  superconductors, *J. Phys. Soc. Jpn.* **81**, 011005 (2012).
- [65] W. O. Tromp, T. Benschop, J.-F. Ge, I. Battisti, K. M. Bastiaans, D. Chatzopoulos, A. Vervloet, S. Smit, E. van Heumen, M. S. Golden, Y. Huang, T. Kondo, Y. Yin, J. E. Hoffman, M. A. Sulangi, J. Zaanen, and M. P. Allan, Puddle formation, persistent gaps, and non-mean-field breakdown of superconductivity in overdoped  $(\text{Pb,Bi})_2\text{Sr}_2\text{CuO}_{6+\delta}$ , [arXiv:2205.09740](https://arxiv.org/abs/2205.09740).
- [66] J. W. Loram, J. L. Tallon, and W. Y. Liang, Absence of gross static inhomogeneity in cuprate superconductors, *Phys. Rev. B* **69**, 060502(R) (2004).

- [67] J. Bobroff, H. Alloul, S. Ouazi, P. Mendels, A. Mahajan, N. Blanchard, G. Collin, V. Guillen, and J.-F. Marucco, Absence of Static Phase Separation in the High  $T_c$  Cuprate  $\text{YBa}_2\text{Cu}_3\text{O}_{6+y}$ , *Phys. Rev. Lett.* **89**, 157002 (2002).
- [68] G. Kim, K. S. Rabinovich, A. V. Boris, A. N. Yaresko, Y. E. Suyolcu, Y.-M. Wu, P. A. van Aken, G. Christiani, G. Logvenov, and B. Keimer, Optical conductivity and superconductivity in highly overdoped  $\text{La}_{2-x}\text{Sr}_x\text{CuO}_4$  thin films, *Proc. Natl. Acad. Sci. USA* **118**, e2106170118 (2021).
- [69] C. N. Breiø, P. J. Hirschfeld, and B. M. Andersen, Supercurrents and spontaneous time-reversal symmetry breaking by nonmagnetic disorder in unconventional superconductors, *Phys. Rev. B* **105**, 014504 (2022).
- [70] V. J. Emery and S. A. Kivelson, Importance of phase fluctuations in superconductors with small superfluid density, *Nature* **374**, 434 (1995).
- [71] G. Kresse and D. Joubert, From ultrasoft pseudopotentials to the projector augmented-wave method, *Phys. Rev. B* **59**, 1758 (1999).
- [72] J. P. Perdew, K. Burke, and M. Ernzerhof, Generalized Gradient Approximation Made Simple, *Phys. Rev. Lett.* **77**, 3865 (1996).
- [73] <https://icsd.products.fiz-karlsruhe.de>.
- [74] A. A. Mostofi, J. R. Yates, Y.-S. Lee, I. Souza, D. Vanderbilt, and N. Marzari, Wannier90: A tool for obtaining maximally localized Wannier functions, *Comput. Phys. Commun.* **178**, 685 (2008).